

To appear in the *Astrophysical Journal*

## The Two-Phase Pair Corona Model for Active Galactic Nuclei and X-ray Binaries: How to Obtain Exact Solutions

Juri Poutanen and Roland Svensson

Stockholm Observatory, S-133 36 Saltsjöbaden, Sweden; juri@astro.su.se, svensson@astro.su.se

### ABSTRACT

We consider two phase accretion disk-corona models for active galactic nuclei and some X-ray binaries. We describe in detail how one can exactly solve the polarized radiative transfer and Comptonization using the iterative scattering method, while simultaneously solving the energy and pair balance equation for both the cold and hot phases. We take into account Compton scattering, photon-photon pair production, pair annihilation, bremsstrahlung, and double Compton scattering, as well as exact reflection from the cold disk. We consider coronae having slab geometry as well as coronae consisting of one or more well separated active regions of cylinder or hemisphere geometry.

The method is useful for determining the spectral intensity and the polarization emerging in different directions from disk-corona systems. The code is tested against a Monte-Carlo code. We also compare with earlier, less accurate, work. The method is more than an order of magnitude faster than applying Monte Carlo methods to the same problem and has the potential of being used in spectral fitting software such as XSPEC.

*Subject headings:* accretion disks – galaxies: Seyfert – gamma rays: theory – polarization – radiative transfer – X-rays: general

### 1. Introduction

Both active galactic nuclei (AGN) and certain X-ray binaries (the galactic black hole candidates, GBHC) show X-ray spectra extending into the hard X-rays (e.g. Mushotzky, Done, & Pounds 1993; Tanaka & Levin 1995). The X-ray spectra of Seyfert 1 galaxies show at least two components: 1) an intrinsic power law component with an intensity index,  $\alpha \sim 0.9 - 1.0$ , in the 2-18 keV range and a spectral cutoff at a few hundred keV (Zdziarski et al. 1994; Madejski et al. 1995; Zdziarski et al. 1995), and 2) a superimposed reflection component arising from reflection and reprocessing of the intrinsic power law by cold opaque matter subtending  $\sim 1-2 \pi$  solid angle as viewed from the X-ray source (e.g. Nandra & Pounds 1994). GBHC such as Cyg X-1 and

1E1740.7-2942 show power law spectra extending up to hundreds of keV (e.g. Gilfanov et al. 1994; Tanaka & Levin 1995). The characteristic features of reflection have been seen in GBHC as well (e.g. Done et al. 1992).

AGN and GBHC are believed to be powered by accretion through an accretion disk. In the unified model for AGN (e.g. Antonucci 1993), it is believed that we are viewing the disks in Seyfert 1 galaxies more or less face on, while for Seyfert 2 galaxies we are viewing the disk more or less edge on through a molecular torus. In GBHC sources we are viewing the binary system along some given (possibly time dependent) direction. The X-ray spectra indicate the existence of both hot X-ray emitting and cold reflecting gas components. The exact geometry is not known, but a currently popular model is the two-phase disk-corona model (e.g. Haardt & Maraschi 1991, 1993, hereafter HM93). The black body disk radiation from the cold disk (in the EUV for AGN, and in the soft X-rays for GBHC) enters the hot corona from one side and gets Comptonized into the X-rays. Part of this X-ray radiation is incident on the cold disk and is partly reflected but mainly reprocessed into soft black body radiation. The remaining part forms the X-ray spectrum leaving the disk-corona system. Both the black body and the Comptonized spectrum are anisotropic so observers at different viewing angles see different spectra (HM93). It immediately clear that such models are neither homogeneous nor spherically symmetric. In order to correctly interpret observed X-ray spectra of AGN and GBHC one needs to know the theoretical spectra for mildly relativistic temperature and for different viewing angles.

Theoretical Comptonized spectra have been computed for two decades now. Almost all work make simplifying assumptions that render them useless for interpreting X-ray spectra from sources were anisotropic effects are important. We briefly discuss standard methods for modeling Comptonized spectra from AGN and GBHC at mildly relativistic temperatures.

One approach is to treat the photon and pair producing processes as well as the energy and pair balance in great detail, but to make large simplifications regarding the radiative transfer using various prescriptions for the spectral shape and using simple escape probabilities to get the photon density (e.g. Zdziarski 1985; Pietrini & Krolik 1995). Such calculations can only give very approximate relations between the typical spectral shape and other parameters.

Other approaches are to do detailed radiative transfer using Monte Carlo methods for geometries such as slabs or spheres (e.g. Hua & Titarchuk 1995) or to improve the analytical theory of Comptonization (e.g. Titarchuk 1994). Normally the following simplifications are made: 1) processes other than Comptonization are neglected, 2) pair balance is not imposed, 3) angle dependence of output spectra is not considered, 4) the soft photon injection is homogeneous throughout the source. There are some exceptions. For example, Skibo et al. (1995) includes bremsstrahlung, pair production, and pair balance, and Zdziarski et al. (1994) assume the soft photons to be injected at one of the slab surfaces. Most work neglect reflection by cold matter. The few papers considering polarized radiative transfer (e.g. Sunyaev & Titarchuk 1985; Haardt & Matt 1993) use the Rayleigh matrix, which is not valid for temperatures and photon energies

above 50 keV.

Pioneering steps were taken by Haardt & Maraschi (1991, 1993) and Haardt (1993, 1994) to solve for angle-dependent spectra from disk-corona systems including reflection as well as energy and pair balance. The method treated the first scattering order accurately, but assumed higher order scatterings to be isotropic. Compton recoil was neglected and therefore the spectral cutoff at photon energies around and above  $kT_e$  could not be treated. Furthermore, the pair balance treatment was approximate as they adopted the semi-analytical theory of Zdziarski (1985) using prescribed spectra. Finally, when determining the reflected spectrum they assumed the X-ray intensity incident on the cold matter to be isotropic. Further steps were taken by Stern et al. (1995a, b) who used nonlinear Monte Carlo techniques to treat disk-corona systems with different inhomogeneous coronal geometries. Here, exact pair balance was imposed throughout the coronal region. Furthermore, output spectra (including the cutoff) had sufficiently good statistics to allow the dependence on the viewing angle to be studied. These work found that anisotropic effects are very important for spectra from disk-corona systems. At mildly relativistic temperatures the first order scattering of the soft disk radiation is suppressed in the face-on direction. This causes the face-on spectrum to be harder up to the spectral peak of the second order scattering, where an *anisotropy break* appears. Above the break the Comptonized spectrum in all directions resembles the angle-averaged one. As shown in Stern et al. (1995b), the anisotropy break easily appears in the 2–18 keV range making  $\alpha_{2–18}$  strongly dependent on viewing angle. The reflection component is also strongly anisotropic (e.g. Matt 1993; Magdziarz & Zdziarski 1995; Poutanen, Nagendra, & Svensson 1996).

The disadvantages with the nonlinear Monte Carlo method is that it is computer intensive requiring more than one hour per run on a Sparc 20. In order to be able to do spectral fitting of observed spectra one needs a much faster method to compute accurate angle dependent spectra from disk-corona systems. In the present paper we describe such a fast code based on the iterative scattering method, i.e. where the radiative transfer equation is solved for each scattering order (e.g. Sunyaev & Titarchuk 1985). Most important radiation processes and photon-photon pair production are included. Energy and pair balance can be imposed. The reflection is accurately treated accounting for the full angular dependence of the incident spectrum (Poutanen et al. 1996). Both slab, cylinder, and hemisphere geometries of the corona can be treated. Finally, the radiative transfer is polarized, both as regards the Comptonization and the reflection. The code has already been used to interpret the statistics of observed X-ray spectral indices and compactnesses from Seyfert 1 galaxies (Stern et al. 1995b). The purpose of the present paper is to fully document the methods used in the code in a selfcontained way.

In the remainder of the paper, we first describe the setup of the two-phase disk-corona model in § 2. The methods of solving the radiative transfer equation in different geometries are considered in § 3. The energy and pair balance and details of the iteration procedure are considered in § 4. We compare our results with those of other available codes in § 5, where we also consider the accuracy and efficiency of various approximations that can be employed in order to decrease the

computing time. Finally, we summarize our work in § 6. Expressions for the reaction rates and redistribution functions (i.e. the Compton redistribution matrix) are given in the Appendices.

## 2. Setup

We consider the simple two-phase disk-corona model, where a hot corona is located above an optically thick plane-parallel cold slab (“disk”) (e.g. Haardt & Maraschi 1991, 1993; Haardt, Maraschi, & Ghisellini 1994). The hot corona is either a plane-parallel slab (with vertical thickness  $H$ ), or an active region with the shape of a hemisphere (with radius  $R$ ), or a cylinder (with vertical height,  $H$ , and horizontal radius,  $R$ ). We allow energy dissipation in both the corona and the cold disk. The radiation escaping from the cold disk consists of a soft component, and a reflected component. The soft flux is equal to the sum of the absorbed incident flux from the corona, and the flux due to local energy dissipation in the cold disk. The spectral shape of these soft components is assumed to be Planckian with temperatures  $T_{\text{bb}}$  and  $T_{\text{disk}}$ , respectively (note that  $T_{\text{bb}} > T_{\text{disk}}$ ). The shape of the reflected component is determined by the shape of incident coronal X-ray radiation (mainly resulting from Comptonization of the soft disk radiation) and the effects of photoelectric absorption and Compton scattering in the cold disk (see, e.g., White, Lightman, & Zdziarski 1988; Magdziarz & Zdziarski 1995).

We can treat coronae both with or without pairs. In this paper, we mostly consider the case of a pure pair corona without any background plasma. The pure pair corona is a consequence of photon-photon pair production above the cold disk. The electrons and positrons are assumed to have a relativistic Maxwellian distribution of the same temperature,  $\Theta = kT_{\text{e}}/m_{\text{e}}c^2$ . The corona is assumed to be uniform in temperature and pair density, and pair escape is neglected. If all power is dissipated in the corona then, for a given geometry, the two parameters: the total power dissipated in corona,  $L_{\text{diss}}$ , and the temperature,  $T_{\text{bb}}$ , of the reprocessed radiation, uniquely determine the optical depth,  $\tau_{\text{T}}$ , and the coronal temperature,  $\Theta$ . If the radiation produced internally in the disk is not negligible, then two more parameters are important: the disk temperature,  $T_{\text{disk}}$ , and the ratio,  $d = L_{\text{disk}}/L_{\text{diss}}$ , where  $L_{\text{disk}}$  is the luminosity that is produced internally in the disk and that enters the corona. For all geometries,  $\tau_{\text{T}}$  is defined as the total vertical Thomson optical depth of the corona (along the symmetry axis in the case of hemisphere geometry).

To solve the pair balance equation, the energy balance equations for the cold and hot phases, and the radiative transfer in the corona self-consistently, we make use of an iteration procedure. To reduce computing time we choose to fix  $\Theta$ , which allow us to compute the thermal Compton redistribution matrix and cross section, and the coronal emissivities for pair annihilation and bremsstrahlung before doing the iterations. We then adjust  $\tau_{\text{T}}$  and  $L_{\text{diss}}$  until the radiation spectra from solving the radiative transfer satisfy the energy balance equations and the pair balance.

When solving the radiative transfer/Comptonization problem, we account for the angular anisotropy of the radiation as well as its polarization properties. The reprocessing in the cold

disk is described by Green's matrix (consisting of four Green's functions) for reflection, where we fully account for the Compton effect, photoelectric absorption, and iron fluorescence, as well as for the angular and polarization properties of the radiation incident on the cold disk (Poutanen et al. 1996). We reduce the time needed to compute the reflection spectrum substantially using the precalculated Green's matrix and achieve better accuracy than all previous treatments of the problem (e.g., White et al. 1988; Magdziarz & Zdziarski 1995).

As additional photon sources and cooling processes of the corona, we consider electron-electron, positron-positron, and electron-positron bremsstrahlung, double Compton scattering, and pair annihilation. We also account for photon absorption due to pair production, which can be important in determining the spectral shapes at pair producing energies ( $h\nu > m_e c^2$ ) and, thus, in influencing the pair balance.

The radiative transfer equation is solved by expanding the radiation field in scattering orders (the iterative scattering method, e.g. Sunyaev & Titarchuk 1985). The intensity in a slab-corona is a function of vertical position (i.e. the Thomson optical depth variable,  $\tau$ ), zenith angle and frequency but is azimuth-independent. In an active region, the intensity, of course, depends on the distance from the symmetry axis and the azimuth angle making the spatial part of the problem two-dimensional. However, by averaging the radiation field over horizontal layers in the active region, we convert the 2D-problem into a 1D-problem suitable for our 1D-code. We discuss the accuracy of this conversion in § 5.

In the pair balance, we use a volume-averaged pair production rate. In the energy balance equations, we need the total luminosities emerging from the cold and the hot phases. Therefore we compute and sum the radiative fluxes emerging from all surfaces of the disk and the corona accounting for all radiative transfer effects.

### 3. Radiative Transfer

#### 3.1. Radiative Transfer in a Slab Corona

Due to azimuthal symmetry and the absence of sources of circular polarization, the radiation field and the degree of polarization at vertical position  $z$  can be fully described by a Stokes vector consisting of two Stokes parameters (Chandrasekhar 1960)  $\tilde{I} = \tilde{I}(z, x, \mu) = (I, Q)^T$ , where  $T$  denotes the transposed vector. The radiative transfer equation describing the propagation of polarized light through a plane-parallel electron (and positron) atmosphere in steady-state can be written in the following form:

$$\mu \frac{d\tilde{I}(z, x, \mu)}{dz} = -(n_e \sigma_{cs}(x) + \alpha_{\gamma\gamma}(z, x, \mu))\tilde{I}(z, x, \mu) + n_e \sigma_T \tilde{S}(z, x, \mu) + \epsilon(x), \quad (1)$$

where  $x \equiv h\nu/m_e c^2$  is the photon energy,  $n_e = n_+ + n_-$  is the total electron and positron density,  $\mu$  is the cosine angle between the slab normal and the direction of photon propagation,  $\sigma_{cs}(x) \text{ cm}^2$  is the

thermal Compton scattering cross section,  $\sigma_T \text{ cm}^2$  is the Thomson cross section,  $\alpha_{\gamma\gamma}(z, x, \mu) \text{ cm}^{-1}$  is the absorption coefficient due to photon-photon pair production, and  $\tilde{S}(z, x, \mu)$  is the electron scattering source function. The emissivity,  $\epsilon(x) = \epsilon_{++} + \epsilon_{--} + \epsilon_{+-} + \epsilon_{-+} + \epsilon_{\text{ann}} + \epsilon_{\text{DC}}$  erg cm $^{-1}$  s $^{-1}$  sr $^{-1}$ , which is assumed to be isotropic and homogeneous, includes all photon sources in the atmosphere, in our case electron-electron, positron-positron, electron-positron bremsstrahlung, annihilation, and double Compton radiation. The expressions for the emissivities and absorption coefficients are given in the Appendices.

Using the following notation for the dimensionless intensity, source function, emissivities, scattering cross section and absorption coefficient:

$$I' = I \frac{H\sigma_T}{m_e c^3}, \quad S' = S \frac{H\sigma_T}{m_e c^3}, \quad \epsilon' = \epsilon \frac{H}{n_e m_e c^3}, \quad \sigma'_{\text{cs}} = \frac{\sigma_{\text{cs}}}{\sigma_T}, \quad \alpha'_{\gamma\gamma} = \frac{\alpha_{\gamma\gamma}}{n_e \sigma_T},$$

and removing the primes, the radiative transfer equation can be written in the following dimensionless form:

$$\mu \frac{d\tilde{I}(\tau, x, \mu)}{d\tau} = -(\sigma_{\text{cs}}(x) + \alpha_{\gamma\gamma}(\tau, x, \mu))\tilde{I}(\tau, x, \mu) + \tilde{S}(\tau, x, \mu) + \epsilon(x), \quad (2)$$

where  $d\tau = \sigma_T n_e dz$  is the differential Thomson optical depth. Hereafter we will only use dimensionless quantities (except in the Appendices).

The Thomson optical depth of the slab is  $\tau_T = H\sigma_T n_e$ . The boundary conditions at the upper and lower surface of the slab are:

$$\begin{aligned} \tilde{I}(\tau = \tau_T, x, -\mu) &= 0, \quad \mu > 0, \\ \tilde{I}(\tau = 0, x, \mu) &= \tilde{I}_{\text{in}}(x, \mu), \end{aligned} \quad (3)$$

i.e. there is no radiation incident at the upper surface, and the radiation incident at the lower surface consists of a reflected component, a soft reprocessed component, and a soft component internally produced in the disk:

$$\tilde{I}_{\text{in}}(x, \mu) = \tilde{I}_{\text{refl}}(x, \mu) + c_{\text{bb}} B_x(T_{\text{bb}}) + c_{\text{disk}} B_x(T_{\text{disk}}). \quad (4)$$

The reflected radiation,  $\tilde{I}_{\text{refl}}(x, \mu)$ , from the cold disk can be found as a convolution of a reflection matrix (Green's matrix)  $\hat{G}(x, \mu; x_1, \mu_1)$  with the incident radiation:

$$\tilde{I}_{\text{refl}}(x, \mu) = \int_x^\infty dx_1 \int_0^1 d\mu_1 \hat{G}(x, \mu; x_1, \mu_1) \tilde{I}(\tau = 0, x_1, -\mu_1). \quad (5)$$

The Green's matrix maps incoming radiation at  $(x_1, -\mu_1)$  into reflected radiation at  $(x, \mu)$ . To compute Green's matrix we use the method developed by Poutanen et al. (1996). The normalization constants in front of the Planckian functions in equation (4) are determined by normalizing the black-body flux to the soft compactnesses,  $l_{\text{repr}}$  and  $l_{\text{disk}}$  (to be defined in § 4.1), as:

$$c_{\text{bb}} \pi \int_0^\infty dx B_x(T_{\text{bb}}) = l_{\text{repr}}; \quad c_{\text{disk}} \pi \int_0^\infty dx B_x(T_{\text{disk}}) = l_{\text{disk}}. \quad (6)$$

The thermal electron scattering source function,  $\tilde{S}(\tau, x, \mu)$ , can be expressed in terms of the azimuthal-averaged Compton redistribution matrix (see e.g. Poutanen & Vilhu 1993):

$$\tilde{S}(\tau, x, \mu) = x^2 \int_0^\infty \frac{dx_1}{x_1^2} \int_{-1}^1 d\mu_1 \begin{pmatrix} R_{11} & R_{12} \\ R_{21} & R_{22} \end{pmatrix} \tilde{I}(\tau, x_1, \mu_1), \quad (7)$$

or in operator form as

$$\tilde{S} = \mathbf{R} \tilde{I}. \quad (8)$$

The factor  $x^2/x_1^2$  in equation (7) appears because we use the photon intensity instead of the photon occupation number to describe the radiation field (see Nagirner & Poutanen 1994). Expressions for the redistribution functions  $R$  are given in Appendix A.1.

We solve the integro-differential equation (2) by expanding the Stokes vector  $\tilde{I}$  in scattering orders (Neumann series):

$$\tilde{I} = \sum_{k=0}^{\infty} \tilde{I}_k, \quad (9)$$

where  $\tilde{I}_k$  is the Stokes vector for photons having undergone  $k$  scatterings (see, e.g., Sunyaev & Titarchuk 1985). This expansion converges quickly for sufficiently small optical depths ( $\tau_T \lesssim 1$ ). The source function for the non-scattered component consist of the flux incident on the corona at the bottom surface,  $\tau = 0$ , and of the internal coronal sources:

$$\tilde{S}_0(\tau, x, \mu) = \mu \tilde{I}_{\text{in}}(x, \mu) H(\mu) \delta(\tau) + \epsilon(x) \quad (10)$$

where  $H(\mu)$  is the Heaviside function. The Stokes vectors,  $\tilde{I}_k^\pm(\tau, x, \mu) = \tilde{I}_k(\tau, x, \pm\mu)$ , for the upward and downward radiation and for all scattering orders  $k \geq 0$  are calculated employing the iteration formulae:

$$\tilde{I}_k^+(\tau, x, \mu) = \int_0^\tau \frac{d\tau'}{\mu} \tilde{S}_k(\tau', x, \mu) \exp \left\{ - \int_{\tau'}^\tau \sigma(\tau'', x, \mu) \frac{d\tau''}{\mu} \right\}, \quad (11)$$

$$\tilde{I}_k^-(\tau, x, \mu) = \int_\tau^{\tau_T} \frac{d\tau'}{\mu} \tilde{S}_k(\tau', x, -\mu) \exp \left\{ - \int_\tau^{\tau'} \sigma(\tau'', x, -\mu) \frac{d\tau''}{\mu} \right\}, \quad (12)$$

where  $\sigma(\tau, x, \mu) = \sigma_{\text{cs}}(x) + \alpha_{\gamma\gamma}(\tau, x, \mu)$ . Using equation (8) the source function can be written as:

$$\tilde{S}_{k+1} = \mathbf{R} \tilde{I}_k. \quad (13)$$

This procedure gives the dependence of the Stokes parameters on frequency, angle and optical depth. Iterative methods where the calculations of the spectral structure and of the angular polarization structure of the radiation field were separated (Sunyaev and Titarchuk 1985; Phillips and Mészáros 1986) fail to obtain the frequency dependence of the Stokes vectors for a given scattering order. Substituting  $\tau = \tau_T$  into equation (11), and  $\tau = 0$  into equation (12), we obtain the emergent Stokes vectors.

### 3.2. Radiative Transfer in Cylinders

In order to treat radiative transfer in cylindrical geometry we divide the cylinder into horizontal spatial layers and average the computed radiation field over each layer (over the radius and the azimuthal directions) leaving only the dependence on the zenith angle. To simplify the calculations we assume the soft (reprocessed and internally produced in the cold disk) and reflected radiation to enter uniformly at the base of the cylinder. Thus, we effectively convert the 2D-problem into a 1D-problem.

The boundary conditions are the same as in the slab case, but the radiation incident on the base of the cylinder is now:

$$\tilde{I}_{\text{in}}(x, \mu) = g\tilde{I}_{\text{refl}}(x, \mu) + c_{\text{bb}}B_x(T_{\text{bb}}) + c_{\text{disk}}B_x(T_{\text{disk}}). \quad (14)$$

The parameter  $g$  is the fraction of the reprocessed and reflected radiation from the cold disk that enters the active region. In the case of slab geometry,  $g = 1$ . For cylinders atop a cold disk  $g \approx 0.6$  if the vertical  $\tau_T$  equals the radial  $\tau_R = Rn_e\sigma_T$ , while  $g \approx 0.45$  for  $\tau_T = 2\tau_R$ . The parameter  $g$  is smaller for active regions detached from the cold disk. The normalization constants,  $c_{\text{bb}}$  and  $c_{\text{disk}}$ , are given by:

$$c_{\text{bb}}\pi \int_0^\infty dx B_x(T_{\text{bb}}) = gl_{\text{repr}}/\pi; \quad c_{\text{disk}}\pi \int_0^\infty dx B_x(T_{\text{disk}}) = l_{\text{disk}}/\pi. \quad (15)$$

The expressions connecting the radiation field inside the cylinder with the source function are analogous to equations (11) and (12):

$$\tilde{I}_k^+(\tau, x, \mu) = \int_0^\tau \frac{d\tau'}{\mu} \tilde{S}_k(\tau', x, \mu) \exp \left\{ - \int_{\tau'}^\tau \sigma(\tau'', x, \mu) \frac{d\tau''}{\mu} \right\} C_+^I(\tau, \tau', \mu), \quad (16)$$

$$\tilde{I}_k^-(\tau, x, \mu) = \int_\tau^{\tau_T} \frac{d\tau'}{\mu} \tilde{S}_k(\tau', x, -\mu) \exp \left\{ - \int_\tau^{\tau'} \sigma(\tau'', x, -\mu) \frac{d\tau''}{\mu} \right\} C_-^I(\tau, \tau', \mu), \quad (17)$$

where the correction factors,  $C_\pm^I$ , reduce the contributions from the source function at  $\tau'$  to the radiation field at  $\tau$  as compared to the slab case (note that  $\mu > 0$ ):

$$C_\pm^I(\tau, \tau', \mu) = \begin{cases} 0, & \text{if } t \geq 1, \\ \frac{2}{\pi} \left( \arccos t - t\sqrt{1-t^2} \right), & \text{if } t \leq 1, \end{cases} \quad (18)$$

$$t = \sqrt{1-\mu^2}|\tau - \tau'|/(\mu 2\tau_R). \quad (19)$$

The equation for the source function (13) remains unchanged.

The emerging (polarized) flux consists of two parts: first, the radiation emerging through the top and the bottom of the cylinder, and, second, the radiation emerging through the vertical surface. The first part can trivially be found from equation (16) by multiplying the emerging intensity with  $\mu\pi$  ( $\pi$  appears because of the definition of the compactness). The second part is

given by:

$$\tilde{F}_k^{\text{side},+}(x, \mu) = \frac{1}{\tau_R} \int_0^{\tau_T} d\tau \int_0^\tau \frac{d\tau'}{\mu} \tilde{S}_k(\tau', x, \mu) \exp \left\{ - \int_{\tau'}^\tau \sigma(\tau'', x, \mu) \frac{d\tau''}{\mu} \right\} C_+^E(\tau, \tau', \mu), \quad (20)$$

$$\tilde{F}_k^{\text{side},-}(x, \mu) = \frac{1}{\tau_R} \int_0^{\tau_T} d\tau \int_\tau^{\tau_T} \frac{d\tau'}{\mu} \tilde{S}_k(\tau', x, -\mu) \exp \left\{ - \int_\tau^{\tau'} \sigma(\tau'', x, -\mu) \frac{d\tau''}{\mu} \right\} C_-^E(\tau, \tau', \mu) \quad (21)$$

where

$$C_\pm^E(\tau, \tau', \mu) = 2\sqrt{1 - \mu^2} \sqrt{1 - t^2}, \quad \text{if } t < 1, \quad (22)$$

and equal to zero otherwise,  $t$  is given by equation (19).

### 3.3. Radiative Transfer in Hemispheres

In the case of hemisphere geometry, we average over the horizontal layers just as we did for cylinder geometry. The incident radiation is given by equations (14) and (15), where the parameter  $g \approx 0.7$  for hemispheres atop the cold disk. The expressions (16) and (17) connect the radiation field inside the hemisphere with the source function with correction factors  $C_\pm^I$  being given by:

$$C_+^I(\tau, \tau', \mu) = \begin{cases} 0, & \text{if } t \geq r + r', \\ 1, & \text{if } t \leq r' - r, \\ C^I, & \text{if } r' - r \leq t \leq r + r', \end{cases} \quad (23)$$

$$C_-^I(\tau, \tau', \mu) = \begin{cases} 0, & \text{if } t \geq r + r', \\ (r'/r)^2, & \text{if } t \leq r - r', \\ C^I, & \text{if } r - r' \leq t \leq r + r', \end{cases} \quad (24)$$

where

$$t = \sqrt{1 - \mu^2} |\tau - \tau'|/\mu, \quad r = \sqrt{\tau_T^2 - \tau^2}, \quad r' = \sqrt{\tau_T^2 - \tau'^2},$$

and

$$\begin{aligned} C^I &= \frac{1}{\pi r^2} \left[ r^2 \phi_* + r'^2 \cos^{-1} \left( \frac{r'^2 - r^2 + t^2}{2r't} \right) - rt \sin \phi_* \right], \\ \phi_* &= \cos^{-1} \left( \frac{r^2 - r'^2 + t^2}{2rt} \right). \end{aligned} \quad (25)$$

The emerging flux through the base of the hemisphere is  $\mu\pi I^-(\tau = 0, x, \mu)$ . The flux through the curved hemisphere surface is given by equations (20) and (21), where  $C_\pm^E$  are (note that  $\tau_T = \tau_R$  and  $\mu > 0$ ):

$$C_+^E(\tau, \tau', \mu) = \begin{cases} 0, & \text{if } t \geq r + r', \\ 2\pi\mu\tau/\tau_T, & \text{if } t \leq r' - r, \\ C_+, & \text{if } r' - r \leq t \leq r + r', \end{cases} \quad (26)$$

$$C_-^E(\tau, \tau', \mu) = \begin{cases} 0, & \text{if } t \geq r + r', \text{ or } t \leq r - r', \\ C_-, & \text{if } r - r' \leq t \leq r + r', \end{cases} \quad (27)$$

$$\begin{aligned}
 C_{\pm} &= 2 \left[ \pm \mu \phi_{\pm} \tau / \tau_T + \sqrt{1 - \mu^2} \sqrt{1 - (\tau / \tau_T)^2} \sin \phi_{\pm} \right], \\
 \phi_+ &= \begin{cases} \phi_*, & \text{if } \mu \geq \sqrt{1 - (\tau / \tau_T)^2}, \\ \min\{\pi/2, \phi_*\}, & \text{if } \mu < \sqrt{1 - (\tau / \tau_T)^2}, \end{cases} \\
 \phi_- &= \phi_*. \tag{28}
 \end{aligned}$$

### 3.4. Isotropic Source Function Approximation

In some applications where high accuracy is not needed and we are not interested in the polarization of the radiation, we can substantially reduce the computing time assuming that the source function,  $S_k(\tau, x, \mu)$ , is isotropic and homogeneous for scattering orders  $k \geq 2$ . The accuracy of this approximation is discussed in § 5.2. The approximation works because for the optically thin coronae photons scattered more than a few times are almost isotropic and are distributed almost homogeneously throughout the medium. In this case, the iteration procedure starting from the second scattering order can be written as follows:

$$S_{k+1}(x) = x^2 \int_0^\infty \frac{dx_1}{x_1^2} R(x, x_1) J_k(x_1), \tag{29}$$

$$J_{k+1}(x) = S_{k+1}(x) P_J(x), \quad k \geq 1, \tag{30}$$

where

$$J_k(x) = \frac{1}{\tau_T} \int_0^{\tau_T} d\tau \frac{1}{2} \int_{-1}^1 d\mu I_k(\tau, x, \mu) \tag{31}$$

is the intensity averaged over optical depth and angles, and

$$R(x, x_1) = \int_0^1 d\mu \int_0^1 d\mu_1 [R_{11}(x, \mu; x_1, \mu_1) + R_{11}(x, \mu; x_1, -\mu_1)] \tag{32}$$

is the angle averaged Compton redistribution function. The quantity,  $P_J(x)$ , can be obtained from equations (16) and (17):

$$\begin{aligned}
 P_J(x) &= \frac{1}{\tau_T} \int_0^{\tau_T} d\tau \frac{1}{2} \int_0^1 \frac{d\mu}{\mu} \left[ \int_0^\tau d\tau' \exp \left\{ - \int_{\tau'}^\tau \sigma(\tau'', x, \mu) \frac{d\tau''}{\mu} \right\} C_+^I(\tau, \tau', \mu) \right. \\
 &\quad \left. + \int_\tau^{\tau_T} d\tau' \exp \left\{ - \int_\tau^{\tau'} \sigma(\tau'', x, -\mu) \frac{d\tau''}{\mu} \right\} C_-^I(\tau, \tau', \mu) \right]. \tag{33}
 \end{aligned}$$

In the case of slab geometry, where  $C_{\pm}^I = 1$ , and at photon energies,  $x < 1$ , where pair production is not important and hence  $\sigma(\tau, x, \mu) = \sigma_{\text{cs}}(x)$ , this integral can be computed analytically:

$$P_J(x) = \tau_T \frac{1}{\tau_x} \left[ 1 - \frac{1}{\tau_x} \left( \frac{1}{2} - E_3(\tau_x) \right) \right], \tag{34}$$

where  $\tau_x = \tau_T \sigma_{\text{cs}}(x)$  is the frequency dependent optical depth and  $E_3$  is the exponential integral of the third order. For  $\tau_x \ll 1$ , we have

$$P_J(x) \sim \tau_T \frac{1}{2} \left( -\ln \tau_x + \frac{3}{2} - \gamma_E \right), \tag{35}$$

where  $\gamma_E = 0.577216\dots$  is the Euler's constant.

The emergent fluxes through the top and bottom of the cylinder, and through the base of the hemisphere, and from the slab, can be found from equations (16) and (17) where the source functions,  $S_k$ , can now be taken out from the integrals. Corresponding  $\mu$ -dependent multiplicative factors similar to  $P_J(x)$  can be computed before the iteration procedure. Similarly, the emergent fluxes through the side of the cylinder, and through the curved surface of the hemisphere can be found using equations (20) and (21).

## 4. The Balance Equations

### 4.1. The Energy Balance

It is common for problems where pair production is important that the luminosities appear in the form of dimensionless compactnesses. We define the compactnesses in the following way:

1. For an active region (a coronal cylinder or a coronal hemisphere)

A dissipation compactness,  $l_{\text{diss}} \equiv (L_{\text{diss}} H / R^2)(\sigma_T / m_e c^3)$ , characterizes the dissipation with  $L_{\text{diss}}$  being the power providing uniform heating of the active region, and  $R$  being the radius of cylinder, and  $H$  its height. For hemispheres we have  $H = R$ . The soft compactness  $l_s \equiv (L_s H / R^2)(\sigma_T / m_e c^3)$  characterizes the soft (reprocessed plus internally dissipated) luminosity from the cold disk entering the active region;  $l_c \equiv (L_c H / R^2)(\sigma_T / m_e c^3)$  is the coronal compactness corresponding to the total luminosity of Compton scattered radiation and radiation emitted in the corona.

2. For a plane-parallel slab corona

A local dissipation compactness is defined as  $l_{\text{diss}} \equiv (L_{\text{diss}} / H)(\sigma_T / m_e c^3)$  with  $L_{\text{diss}}$  being the power providing uniform heating of a cubic volume of size  $H$  in the slab. Similar definitions hold for  $l_s$  and  $l_c$ .

The soft compactness,  $l_s$ , consist of two parts,  $l_{\text{disk}}$  and  $g l_{\text{repr}}$ , where  $l_{\text{disk}}$  is the compactness of the power that is internally dissipated in the cold disk and that enters the corona, and  $l_{\text{repr}}$  is the compactness of the power reprocessed by the cold disk. The parameter  $g$  is the fraction of the radiation reprocessed and reflected from the cold disk which enters the active region. Introducing the parameter  $d \equiv l_{\text{disk}} / l_{\text{diss}}$ , we can write the energy balance equation for the cold phase as

$$l_s = g l_{\text{repr}} + d l_{\text{diss}}. \quad (36)$$

If all power dissipates in the corona then  $d = 0$ . The total coronal compactness,  $l_c$ , is the sum of the compactness dissipated in the corona,  $l_{\text{diss}}$ , and the part of the soft and reflected compactnesses which is scattered in corona:

$$l_c = l_{\text{diss}} + p_{\text{sc}}(l_s + g l_{\text{refl}}). \quad (37)$$

This equation represents the energy balance of the hot phase (i.e. the corona). Here  $p_{\text{sc}}$  is the probability of scattering in the corona for disk photons entering the base of the active region ( $p_{\text{sc}}$  is a geometry dependent function of  $\tau_{\text{T}}$ ); and  $l_{\text{refl}}$  is the compactness reflected from the cold disk. Introducing the integrated disk albedo,  $a$ , which is the fraction of the incident luminosity reflected by the cold disk, and the anisotropy parameter,  $\eta$ , which is the fraction of all coronal radiation (Comptonized, annihilation, bremsstrahlung, and double Compton radiation) that is incident on the cold disk, we can write:

$$l_{\text{refl}} = a\eta l_c, \quad l_{\text{repr}} = (1 - a)\eta l_c. \quad (38)$$

The equations (36)-(38) can easily be solved for the ratios  $l_c/l_{\text{diss}}$  and  $l_s/l_{\text{diss}}$ :

$$\frac{l_c}{l_{\text{diss}}} = \frac{1 + p_{\text{sc}}d}{1 - p_{\text{sc}}g\eta}, \quad (39)$$

$$\frac{l_s}{l_{\text{diss}}} = \frac{g\eta(1 - a) + d(1 - p_{\text{sc}}g\eta a)}{1 - p_{\text{sc}}g\eta}. \quad (40)$$

Defining the amplification factor,  $A \equiv l_c/l_s$ , we obtain

$$A = \frac{1 + p_{\text{sc}}d}{g\eta(1 - a) + d(1 - p_{\text{sc}}g\eta a)}. \quad (41)$$

If all power dissipates in the corona we have  $A = 1/g\eta(1 - a)$ .

We now show how to compute the parameters entering the energy balance equations from the solution of radiative transfer. Let us define the partial flux emergent from the corona after  $k$  scatterings as (note that  $\mu > 0$ ):

$$\begin{aligned} \tilde{F}_k^+(x, \mu) &= \mu \tilde{I}_k^+(\tau = \tau_{\text{T}}, x, \mu), \\ \tilde{F}_k^-(x, \mu) &= \mu \tilde{I}_k^-(\tau = 0, x, \mu), \end{aligned} \quad (42)$$

for slab geometry. For cylinder geometry, the expressions are the following:

$$\begin{aligned} \tilde{F}_k^+(x, \mu) &\equiv \tilde{F}_k^{\text{side},+}(x, \mu) + \mu\pi \tilde{I}_k^+(\tau = \tau_{\text{T}}, x, \mu), \\ \tilde{F}_k^-(x, \mu) &\equiv \tilde{F}_k^{\text{side},-}(x, \mu) + \mu\pi \tilde{I}_k^-(\tau = 0, x, \mu). \end{aligned} \quad (43)$$

Analogous expressions hold for hemisphere geometry, but the upward flux is just  $\tilde{F}_k^+(x, \mu) = \tilde{F}_k^{\text{side},+}(x, \mu)$ . Let us also define  $\tilde{F}_0^{\text{in},+}$  as the emergent flux of unscattered soft and reflected radiation entering the corona (note that  $\tilde{F}_0^{\text{in},-} = 0$ ). The emergent flux of unscattered radiation emitted in the corona is  $\tilde{F}_0^{\pm}$ . The total emergent coronal flux is then given by  $\tilde{F}_c^{\pm} = \tilde{F}_0^{\pm} + \sum_{k=1}^{\infty} \tilde{F}_k^{\pm}$ , and the total emergent flux is  $\tilde{F}^{\pm} = \tilde{F}_0^{\text{in},\pm} + \tilde{F}_c^{\pm}$ . The total reflected radiation can be found by convolving of Green's matrix for Compton reflection with the total flux incident on the cold disk:

$$\tilde{I}_{\text{refl}}(x, \mu) = \int_x^{\infty} dx_1 \int_0^1 \frac{d\mu_1}{\mu_1} \hat{G}(x, \mu; x_1, \mu_1) \tilde{F}^-(x_1, \mu_1). \quad (44)$$

The integrated disk albedo,  $a$ , is the ratio of the reflected flux to the total flux incident on the cold disk:

$$a = \frac{\int_0^\infty dx \int_0^1 I_{\text{refl}}(x, \mu) \mu d\mu}{\int_0^\infty dx \int_0^1 F^-(x, \mu) d\mu}. \quad (45)$$

The anisotropy parameter,  $\eta$ , is given by

$$\eta = \frac{\int_0^\infty dx \int_0^1 F_c^-(x, \mu) d\mu}{\int_0^\infty dx \int_0^1 [F_c^+(x, \mu) + F_c^-(x, \mu)] d\mu}, \quad (46)$$

and the scattering probability,  $p_{\text{sc}}$ , for slab geometry is given by

$$p_{\text{sc}} = 1 - \frac{\int_0^\infty dx \int_0^1 F_0^{\text{in},+}(x, \mu) d\mu}{\int_0^\infty dx \int_0^1 I_{\text{in}}(x, \mu) \mu d\mu}, \quad (47)$$

with similar expressions for hemisphere and cylinder geometry, but a factor  $\pi$  should then be introduced in the denominator. In the calculations,  $d$  is specified and  $g$  is determined in advance, while  $a$ ,  $\eta$ , and  $p_{\text{sc}}$  are calculated from the radiative transfer results using expressions (45)–(47), and the amplification factor,  $A$ , is given by equation (41).

The sum of  $l_{\text{diss}}$  and  $l_{\text{disk}}$  can be written as the sum of the total upward emergent flux and the total downward emergent flux that does not reenter the corona:

$$l_{\text{diss}} + l_{\text{disk}} = 2\pi \int_0^\infty dx \int_0^1 [F^+(x, \mu) + (1-g)F^-(x, \mu)] d\mu. \quad (48)$$

The actual value of  $l_{\text{diss}}$  is determined by pair balance, but does not influence the energy balance.

#### 4.2. The Pair Balance

For the range of temperatures of interest,  $\Theta < 2$ , particle-particle and particle-photon pair production is negligible compared to photon-photon pair production. The pair annihilation rate,  $\dot{n}_{\text{ann}} \text{ cm}^{-3}$ , is uniform throughout the corona, while the pair production rate,  $\dot{n}_{\gamma\gamma}(\tau) \text{ cm}^{-3}$ , depends on the radiation field inside the medium being largest at the center where the photon density is largest and smallest at the boundaries. In pair balance, the pair annihilation rate,  $\dot{n}_{\text{ann}}$ , is equal to the volume-averaged pair production rate:

$$\dot{n}_{\text{ann}} = \bar{n}_{\gamma\gamma}, \quad (49)$$

where

$$\bar{n}_{\gamma\gamma} = \begin{cases} \frac{1}{\tau_T} \int_0^{\tau_T} \dot{n}_{\gamma\gamma}(\tau) d\tau, & \text{for slabs and cylinders,} \\ \frac{3}{2\tau_T} \int_0^{\tau_T} [1 - (\tau/\tau_T)^2] \dot{n}_{\gamma\gamma}(\tau) d\tau, & \text{for hemispheres.} \end{cases} \quad (50)$$

Here the extra factor in the integrand for hemispheres accounts for the decreasing volume of horizontal layers with height. The expressions for  $\dot{n}_{\text{ann}}$  and  $\dot{n}_{\gamma\gamma}(\tau)$  are given in Appendices A.5 and A.6.

### 4.3. The Iteration Procedure

For a given coronal geometry (slab, cylinder, or hemisphere atop of the cold disk) only two parameters,  $l_{\text{diss}}$  (or, alternatively,  $\Theta$ ) and  $T_{\text{bb}}$ , uniquely specify the simulations if all power is dissipated in corona ( $d = 0$ ). For  $d \neq 0$ , two more parameters,  $d$  and  $T_{\text{disk}}$ , should be specified. The equilibrium state satisfies the energy and pair balance equations coupled with the radiative transfer. To find the solution we make use of an iterative procedure. For a given  $\Theta$ , we compute the Compton redistribution matrix and the cross section, the coronal emissivities (annihilation and bremsstrahlung), and guess the initial values for the  $l_{\text{diss}}$  and  $\tau_{\text{T}}$ . The reflected spectrum and the pair production absorption coefficient are set to be zero. Initial values for the parameters in the energy balance equations are  $a = 0$ ,  $\eta = 1/2$ ,  $p_{\text{sc}} = 0$ . We also compute the amplification factor  $A$ , and the soft compactnesses,  $l_{\text{repr}}$  and  $l_{\text{disk}}$ . We then normalize the incident black body radiation using equations (6) or (15) and thus obtain the incident spectrum,  $\tilde{I}_{\text{in}}(x, \mu)$ , from equations (4) or (14). Solving the radiative transfer by expansion in scattering orders we find the radiation field inside the medium as well as the emergent fluxes. We then compute the rate of pair production and the absorption coefficient, the double Compton emissivity, the reflected spectrum, and the albedo,  $a$ , the parameters  $\eta$ , and  $p_{\text{sc}}$ , and the amplification factor,  $A$ .

By comparing  $\bar{n}_{\gamma\gamma}$  with  $\dot{n}_{\text{ann}}$  we calculate a new imposed dissipation compactness  $l_{\text{diss}}^{\text{new}} = l_{\text{diss}}^{\text{old}} \sqrt{\dot{n}_{\text{ann}} / \bar{n}_{\gamma\gamma}}$ . Comparing the calculated amplification factor  $A^{\text{new}}$  with  $A^{\text{old}}$  we choose the new optical depth,  $\tau_{\text{T}}$ , to be smaller than the old  $\tau_{\text{T}}$  if  $A^{\text{new}} > A^{\text{old}}$ , and larger if  $A^{\text{new}} < A^{\text{old}}$ . The change,  $\Delta\tau_{\text{T}}$ , decreases by a factor of two for on each iteration when the sign  $\Delta\tau_{\text{T}}$  changes. After that we start the next iteration by again solving the radiative transfer.

The number of iterations needed to achieve an accuracy better than 1% in all equations is about 10. On a Sparc 20 a typical simulation takes about 5 minutes for 6 angular points, 7 spatial zones, and 80 frequency points. The isotropic source function approximation (see § 3.4) reduces the computing time for solving the radiative transfer problem by an order of magnitude.

## 5. Comparison with Other Codes

### 5.1. Comparison with Non-Linear Monte-Carlo Results

We compare our calculations based on the iterative scattering method (ISM) with the corresponding results using the Non-Linear Monte-Carlo (NLMC) code by Stern (see Stern et al. 1995a). We made 3 test runs each for slabs and for hemispheres atop of the cold disk. We assume that all power dissipates in the corona ( $d = 0$ ). The parameter  $g$  is calculated in the iteration procedure assuming that only the radiation reprocessed below the base of the active region actually reenters the active region. The results are given in Table 1 and are shown in Figure 1. We find that for a given  $\Theta$ , the optical depth,  $\tau_{\text{T}}$ , is almost the same for both codes with the largest difference being about 5-8 per cent at small  $\tau_{\text{T}}$ . The difference in the derived

compactnesses,  $l_{\text{diss}}$ , is less than 20 per cent for slab geometry. In the case of hemispheres,  $l_{\text{diss}}$  differs by 20 per cent at large  $\tau_T$ , and is a factor two smaller at small  $\tau_T$  due to our approximate treatment of the radiative transfer in hemispheres. The procedure of averaging the radiation field over the horizontal layers artificially increases the photon density in the active region causing pair balance to be reached at smaller compactnesses. For large  $\tau_T$ , the difference is smaller due to smaller boundary effects. The differences can also be due to our assumed homogeneity of the corona, rather than using a number of zones as in the NLMC method. As shown in Figure 1, both codes give quite similar spectral shapes for the emerging radiation for both types of geometries. The differences in  $l_{\text{diss}}$  can be considered as small (at least for the slab case) if we remember that  $\Theta$  and  $\tau_T$  depend rather weakly on  $l_{\text{diss}}$ . Thus, if we fix  $l_{\text{diss}}$  instead of  $\Theta$ , the differences in  $\Theta$  and  $\tau_T$  will be about 2 per cent.

## 5.2. The Accuracy of some Useful Approximations

A number of approximations can be used to decrease the time needed to compute the redistribution function for Compton scattering. One is the isotropic scattering approximation in the electron rest frame (see eq. [A15] in Appendix A.2). We found that for the mildly relativistic temperatures considered here the Comptonization spectra computed in this approximation is very accurate at small energies ( $x < \Theta$ ) but have deficits of photons at higher energies. Solving the pair balance in this approximation gives  $l_{\text{diss}}$  a factor of 6 larger for large  $\tau_T$  (small  $\Theta$ ), and a factor of 2 larger at small  $\tau_T$  (large  $\Theta$ ) (see Table 1 where this approximation is denoted ISOSCAT1).

To improve the high energy behavior of the Comptonized spectra, we used the redistribution function from equation (A15) and the exact value for  $\gamma_*$  from equation (A8). This approximation works much better, but still produces deficit of high energy photons. We found the resulting  $l_{\text{diss}}$  to be 10-30 per cent too large (see Table 1 where this approximation is denoted ISOSCAT2). Spectra in this approximation (dashed curves) are compared with exact results (solid curves) in Figure 2. At low energies ( $x < \Theta$ ) the spectra are almost identical, but the approximate spectra fall more rapidly at larger energies forcing the compactness to increase in order to satisfy the pair balance. Due to the small contribution of photons with  $x \sim 1$  to the total energy balance, the optical depth differs by less than 1 per cent from the exact calculations. We conclude that this approximation is useful for modeling spectra of mildly relativistic pair plasmas.

In many works, the pair production rate is computed assuming an isotropic radiation field. The isotropic pair production cross section,  $R_{\gamma\gamma}^{\text{iso}}(xx_1)$  (see Appendix A.8), is much easier to compute than the angle-dependent pair production cross section,  $R_{\gamma\gamma}(xx_1, \mu, \mu_1)$  (see e.g. Coppi & Blandford 1990). In the problem at hand, the radiation field is strongly anisotropic. We investigated the errors caused by making the radiation field isotropic before computing the pair production rate (see Table 1 where this approximation is denoted ISORAD). The resulting  $l_{\text{diss}}$  are systematically lower than those obtained using the exact angle-dependent  $R_{\gamma\gamma}$ , because of a higher pair production rate for the isotropic case. The effect is smaller at large  $\tau_T$  where the

radiation field is more isotropic. Changes in the pair production rate have no influence on the energy balance and consequently does not change the computed spectra and optical depths. It does, however, influence the value of the compactness.

In § 3.4 we presented a method of solving the radiative transfer equation when the source function is assumed to be isotropic starting from the second scattering order. The overall spectral shapes in this approximation (dotted curves) are quite similar to the exact spectra (solid curves) in Figure 2. The ISOSF approximation underestimates the flux in the “edge-on” direction for hemisphere geometry due to the artificial isotropization of the radiation field. The differences in optical depth are negligible for slab geometry, but become about 3-10 per cent for hemispheres. The resulting  $l_{\text{diss}}$  are 10-50 per cent too large (see Table 1 where this approximation is denoted by ISOSF).

### 5.3. Comparison with HM93

In Figure 3 we compare our calculations with the results from Fig.4a-c in HM93 for slab geometry. In the low energy band they are almost identical, but at high energies ( $x > \Theta$ ) the spectra of HM93 have too sharp cutoffs reflecting their use of an *ad hoc* exponential cutoff  $\exp(-x/\Theta)$ . The actual cutoff energy is approximately  $x \approx 2\Theta$ , and the cutoff is not a true exponential, but rather reflects the thermal Compton scattering kernel and the distribution of the emergent photons over the scattering orders. The spectral indices in the 2 – 18 keV range,  $\alpha_{2-18}$ , are very close (see Table 2) for small  $\Theta$ , but differs at larger  $\Theta$ . The reason probably lies in the treatment of the reflection from the cold disk. HM93 computed the reflection using the Monte-Carlo method assuming isotropic incident flux. For large  $\Theta$ , the *anisotropy break* (see Stern et al. 1995b) occurs in the 2 – 18 keV range. The flux incident on the cold disk is thus very anisotropic having its maximum along the normal to the disk. Making the flux isotropic by angle averaging artificially increases the flux along the plane of the disk, which has a larger probability for reflection (Matt 1993; Poutanen et al. 1996). The contribution of the reflection component to the total flux increases making the 2-18 keV spectra flatter. This explains the difference in  $\alpha_{2-18}$  at large  $\Theta$ .

The  $\Theta-\tau_T$  relation obtained by our code agrees with calculations of HM93 to within a percent or two for small  $\tau_T \approx 0.01$ . The difference increases with increasing  $\tau_T$  and at our largest  $\tau_T = 0.37$  the  $\Theta$  of HM93 is about 10 per cent too large due to our spectral differences and the corresponding influence on the energy balance. The anisotropy factor,  $\eta$ , (see Fig. 2a in HM93) agrees very well up to  $\tau_T = 0.1$ . Above that the  $\eta$  of HM93 is slightly too small, becoming 0.02 smaller at  $\tau_T = 0.37$  most likely due to our  $\Theta$  being 10 per cent smaller. Our albedo,  $a$ , is smaller (0.13 instead of 0.16) at small  $\tau_T$  (see Fig. 2b in HM93). Above  $\tau_T = 0.05$ , our  $a$  is 0.01 larger. The differences are likely due to our use of a fully relativistic and anisotropic treatment of the reflection.

The comparison of compactnesses is not so easy. First of all, HM93 give the values

for the Compton compactness  $l_c$  which is related to the total dissipation compactness as  $l_{\text{diss}} = (1 - p_{\text{sc}}\eta)l_c$ , where  $p_{\text{sc}}$  is the probability of scattering in corona (see § 4.1). Second, they define the compactness to be factor of  $\pi$  larger than our definition. Thus, in Table 2 we give the corrected  $l_{\text{diss}} = (1 - p_{\text{sc}}\eta)l_c/\pi$ , instead of the original values of  $l_c$  from Table 1 in HM93. For small  $\tau_T$ , our compactnesses are a factor 5 smaller, but for  $\tau_T = 0.2$  our compactness is larger than corresponding compactnesses of HM93. The approximate estimates by HM93 of the pair producing photon density inside the slab (see Appendix B in HM93) and the prescription for the Comptonized spectra (Zdziarski 1985) used in the pair balance calculations are responsible for the remaining differences.

#### 5.4. Comparison of Comptonized Spectra with Analytical Formulae

We compare the angle averaged Comptonized spectra computed using the ISM code with the analytical formulae for thermal Comptonization from the papers by Titarchuk (1994, his eqs. [35] and [44]) and Hua & Titarchuk (1995, their eqs. [9] and [10]). We consider monochromatic incident photons with  $h\nu_0 = 8$  eV on the lower boundary of the slab. The only process which is taken into account is Comptonization. No pair or energy balance is imposed. Calculations for three different optical depths and temperatures are presented in Figure 4. All three cases correspond to regime 2 in Hua & Titarchuk (1995). We find that the Hua & Titarchuk formulae rather well represent the general spectral behavior, but give systematically fewer photons in the high energy tail. The Titarchuk formulae, however, give a very good description of the spectra for relatively small temperatures ( $\Theta < 0.2$ ), while they produce too many photons in the Wien bump for larger temperatures. In all these cases we should, however, remember that spectra below the anisotropy break as well as the high energy tail have quite different behavior at different viewing angles. The analytical formulae do not provide this angular dependence of the spectrum, and are therefore quite limited in practice.

#### 5.5. Polarization Properties

In this section, we compare our calculations of the degree of polarization of the radiation emerging from the Compton scattering slab-corona with some earlier results by others. We assume here that the cold disk emits semi-isotropic unpolarized radiation. We define the degree of polarization as  $p = (Q/I) 100\%$ . The polarization is positive when the electric vector is predominantly parallel to the normal to the slab. The behavior of the total polarization is affected by both the Compton scattering radiation from the hot corona, and by reflected radiation from the cold disk.

Sunyaev & Titarchuk (1985) calculated the polarization of the Comptonized radiation from a slab. The angular and polarization structure of the radiation field were obtained with an iteration

procedure based on an expansion in scattering orders using the Rayleigh matrix. The frequency dependence of the intensity was obtained solving the Kompaneets equation (see Sunyaev & Titarchuk 1980), which is a diffusion equation in frequency space. The distribution of photons over escape time and thus the relation between the scattering order and frequency were obtained by solving the diffusion equation in physical space. This approach has a few shortcomings. First, the diffusion approximation in optical depth (i.e. physical space) is not valid for the optically thin coronae considered here. Second, for the case of a hot electron gas, the frequency redistribution cannot be considered as diffusion due to the large frequency shift in each scattering. And last, for high electron temperatures ( $\Theta \gtrsim 0.1$ ) and/or large photon energy ( $x \gtrsim 0.1$ ), the polarization properties of the exact Compton redistribution matrix are quite different from those of the Rayleigh matrix (Poutanen & Vilhu 1993). Thus, even for quite small electron temperature,  $\Theta = 0.11$ , and relatively large optical depth,  $\tau_T = 0.5$ , the maximum polarization of the hard radiation computed by this method is  $p \approx 50\%$  (see Fig. 8 in Sunyaev & Titarchuk 1985, note also that their  $\tau_0 = \tau_T/2$ ), compared to  $p \approx 25\%$  in our calculations (see our Fig. 5). The differences become much larger for smaller  $\tau_T$  and/or larger  $\Theta$ .

Following the same idea of separating the polarization structure from the frequency redistribution, Haardt & Matt (1993) computed the degree of polarization from an optically thin hot slab-corona applying the method of Haardt (1993) to obtain the spectra. Using an iterative scattering scheme similar to ours they avoided the diffusion approximation both in frequency and optical depth space. They, however, still used the Rayleigh matrix. To compare the results, we have chosen the same parameters as in Figure 2 in Haardt & Matt (1993). The blackbody temperature is taken to be,  $T_{bb} = 10$  eV, the optical depth is  $\tau_T = 0.5$  and  $0.05$ . We show the results of our computations in Figures 5 and 6. We present the results for two viewing angles,  $\mu = 0.11$  and  $\mu = 0.50$ . The degree of polarization is zero in the direction normal to the slab due to symmetry. It is clearly seen that the degree of polarization is much too large in Haardt & Matt (1993). They found the maximum polarization to be  $p \approx 45\%$  for  $\tau_T = 0.5$  and  $p \approx 33\%$  for  $\tau_T = 0.05$ , while we obtained  $p \approx 25\%$  and  $p \approx 5\%$ , respectively (thick solid curves in Figs. 5 and 6).

Below, we discuss the polarization properties both of the Comptonized radiation from the hot corona and of the radiation reflected from the cold slab. In order to better see the contribution to the overall polarization from different scattering orders we also show the spectra for individual scattering orders as well as the total spectrum in the upper panels of Figures 5 and 6.

First we consider the polarization caused by scattering in the hot corona. The degree of polarization increases with the number of scatterings reaching its asymptotic value after few scatterings. The asymptotic value depends on optical depth, temperature and zenith angle. At energies close to  $m_e c^2$ , the Klein-Nishina corrections start to be important decreasing the polarization. As the electron temperature increases the polarization decreases (Poutanen & Vilhu 1993). At a given frequency the contribution from the higher scattering orders (with larger polarization) becomes smaller also decreasing the polarization. Due to these two reasons the

polarization in Figure 5 ( $\tau_T = 0.5$ ) is larger than in Figure 6 ( $\tau_T = 0.05$ ). The polarization of a given scattering order first decreases toward higher energies but then increases due to the contribution from the scattered reflected component. The decrease is caused by the fact that the largest energy shift is obtained in backward scatterings which do not produce additional polarization.

The reflection component contributes to the overall spectra at energies  $x \approx 0.01 - 1$ . When the flux incident on the cold disk is nearly isotropic, which is the case for optically thin corona, the polarization of the reflected component is positive at  $x \lesssim 1$ . It is maximal in edge-on directions, and is zero in the normal direction (see Poutanen et al. 1996 for a discussion of the polarization properties of Compton-reflected radiation from the cold slab). The polarization in the direction close to the normal decreases at higher energies, changing sign at  $x \sim 0.6$ . The flux reflected close to the normal direction cuts off at energies above  $x \sim 1$ . At directions closer to the plane of the slab, the cutoff is slower, and is determined by the cutoff of the incident spectrum. The polarization has a sharp feature at 6.4 keV due to the contribution from the unpolarized fluorescent iron line.

For  $\tau_T = 0.5$  (Fig. 5) the polarization of the reflected radiation (and that of the reflected component scattered once or twice in the corona) is smaller than the polarization of the component produced by Compton scatterings in hot corona. This causes the polarization to decrease at  $x > 0.1$ . On the other hand for  $\tau_T = 0.05$  (Fig. 6) the reflected component has significantly larger polarization than the scattered component resulting in a smoothly increasing polarization in the energy interval from  $x \approx 0.01$  up to  $x \sim 0.1$ . The decrease of the polarization of the reflected component at higher energies and the change of sign at  $x \sim 0.6$  for  $\mu = 0.5$  cause the drop in the total polarization at  $x \sim 1$ .

Future observations of X-ray polarization by *Spectrum-X- $\gamma$*  satellite (Kaaret et al. 1992) can be a powerful tool for determining the physical conditions and, probably, the geometry of the X-ray emitting region in AGN and X-ray binaries. We note here that the degree of polarization for hemisphere and cylinder geometries is smaller than for the slab case. We can conclude that if small polarization in the X-rays will be observed this could argue for Comptonization models where the temperature of the electron gas is large and/or for models where the geometry of the corona is not slab-like.

## 6. Summary and Conclusions

We have described a versatile code based on the iterative scattering method (ISM) to accurately solve the radiative transfer and Comptonization in a two-phase disk-corona models for active galactic nuclei and X-ray binaries.

The code has several attractive features some of them being unique to this code:

- 1) The radiative transfer is fully angle-dependent, and one can easily determine the outgoing spectrum in any direction to high accuracy at any photon energy. The outgoing spectrum in a given direction may differ greatly from the angle-averaged spectrum.
- 2) The radiative transfer is valid for both nonrelativistic and relativistic temperatures.
- 3) The radiative transfer is polarized.
- 4) Most important radiation processes in hot thermal plasmas including Compton scattering, photon-photon pair production, pair annihilation, bremsstrahlung, and double Compton scattering are taken into account. The latter two were not important for the parameters of the test cases we considered in this paper.
- 5) The corona can be in energy and/or pair balance.
- 6) The corona can either be a pure pair corona, or one can include a background plasma.
- 7) The reflection by the cold disk is exactly treated using a reflection matrix that, in particular, accounts for the full angular dependence of the incident radiation.
- 8) The ISM code has been extensively tested against a Non-Linear Monte Carlo (NLMC) code (Stern et al. 1995b) finding very good agreement.
- 9) The ISM code is an order of magnitude faster than the NLMC code. The ISM code also allows for an easier determination of the spectral fall-off at photon energies above  $kT_e$ . The ISM code also gives more accurate emerging spectra at a given viewing angle as compared to the NLMC code where one must average over a range of viewing angles in order to improve the photon statistics.
- 10) Various approximations for the radiative transfer/Comptonization can be used in order to improve computing efficiency. Quite accurate results can be obtained if one assumes the Compton scattering source function to be isotropic. The gain in computing efficiency is then an order of magnitude. A typical run on a Sparc 20 then takes about 40 s for three angular, 80 frequency, and 7 spatial gridpoints.

There are, however, some limitations:

- 1) The iterative scattering method converges only for small optical depths. For small temperatures ( $\Theta < 0.1$ ) and large optical depths ( $\tau > 1$ ), the round off errors become large due to the large number of scatterings and the accuracy of the results decreases. The maximum allowed  $\tau_T$  depends on the temperature and is approximately 1 for  $\Theta = 0.1$ , and 1.5 for  $\Theta = 0.5$  in the slab case and 2 – 3 in the case of hemisphere geometry. This is not much of a limitation at temperatures above about 100 keV, as the optical depths needed to explain observed X-ray spectral indices in AGN are necessarily less than unity.
- 2) The ISM code is one-dimensional. The ISM code can, however, be applied to quasi-1D radiative transfer in two-dimensional active regions with cylinder or hemisphere geometry atop or

elevated above the cold disk. The NLMC code can, in principle, treat arbitrary geometries.

3) The corona is uniform in temperature and density. The Nonlinear Monte Carlo code has been used (Stern et al. 1995b) to show that the differences in temperature and density across the corona is at most a factor 2. In principle, one could divide the corona into a few zones, and solve the radiative transfer equation using the appropriate Compton redistribution functions and cross sections corresponding to the temperature in each zone. The pair and energy balance equations should then be solved in each zone separately. This, however, is much more time consuming than considering a homogeneous corona. The resulting spectra from homogeneous and inhomogeneous corona are very similar.

4) The ISM code treats steady radiative transfer. The NLMC code, on the other hand, can treat time dependent situations.

There are several possible applications of the ISM code:

1) Results of earlier work using various approximations can be checked, and the validity of the approximations tested. In particular, we find that the full Compton redistribution matrix, rather than the Rayleigh scattering matrix, must be used in order to obtain accurate polarized X-ray spectra.

2) The validity of published analytical fits for angle-averaged Comptonized spectra can be checked. The results of the ISM code can be used to obtain analytical fits of spectra as function of viewing angle and for different geometries.

3) The ISM code has great potential for modeling X-ray and  $\gamma$ -ray spectra from active galactic nuclei and X-ray binaries. The ISM code has already been used together with a NLMC code to interpret the statistics of observed X-ray spectral indices and compactnesses from Seyfert 1 galaxies (Stern et al. 1995b). The anisotropy of outgoing spectra is an important ingredient in this interpretation, which could not have been done using angle-averaged model spectra.

4) The ISM code is highly suitable for inclusion in spectral fitting software such as XSPEC, whereupon observed X-ray spectra can be modeled. Such modeling of a number of sources will appear in forthcoming work.

5) The ability of the ISM code to treat polarized radiative transfer makes it a powerful tool for interpreting future observations of X-ray polarization from, e.g., the *Spectrum-X- $\gamma$*  and *INTEGRAL* satellites.

The authors thank Boris Stern for stimulating discussions. This research was supported by grants and a postdoctoral fellowship (J.P.) from the Swedish Natural Science Research Council.

## A. Rates of the Physical Processes

### A.1. The Electron Scattering Source Function and the Compton Redistribution Matrix

The thermal electron scattering source function,  $\tilde{S}(\tau, x, \mu)$ , for an azimuth-independent radiation field accounting only for linear polarization can be expressed in terms of the azimuth-averaged Compton redistribution matrix,  $\hat{R}(x, \mu; x_1, \mu_1)$ , as:

$$\tilde{S}(\tau, x, \mu) = x^2 \int_0^\infty \frac{dx_1}{x_1^2} \int_{-1}^1 d\mu_1 \hat{R}(x, \mu; x_1, \mu_1) \tilde{I}(\tau, x_1, \mu_1), \quad (\text{A1})$$

Here,  $\hat{R}$  is the azimuth-averaged product of two rotational matrices,  $\hat{L}$ , and the thermal Compton redistribution matrix,  $\hat{C}(x, x_1, \cos \theta)$  (Poutanen & Vilhu 1993; the hat identifies  $\hat{R}$ ,  $\hat{L}$ , and  $\hat{C}$  as matrices, the tilde identifies  $\tilde{S}$  and  $\tilde{I}$  as vectors):

$$\hat{R}(x, \mu; x_1, \mu_1) = \int_0^{2\pi} d\varphi \hat{L}(-\chi) \hat{C}(x, x_1, \cos \theta) \hat{L}(\chi_1). \quad (\text{A2})$$

In general, it is  $4 \times 4$  matrix. The rotational matrices are given by the following expression (see, e.g., Chandrasekhar 1960):

$$\hat{L}(\chi) = \begin{pmatrix} 1 & 0 & 0 & 0 \\ 0 & \cos(2\chi) & \sin(2\chi) & 0 \\ 0 & -\sin(2\chi) & \cos(2\chi) & 0 \\ 0 & 0 & 0 & 1 \end{pmatrix}. \quad (\text{A3})$$

Due to azimuthal symmetry and the absence of circular polarization we consider only the  $2 \times 2$  matrix in the upper left corner of the general matrix:

$$\hat{R} = \begin{pmatrix} R_{11} & R_{12} \\ R_{21} & R_{22} \end{pmatrix}. \quad (\text{A4})$$

The elements of this matrix are:

$$\begin{aligned} R_{11} &= \int C d\varphi, \\ R_{12} &= \int C_I \cos 2\chi_1 d\varphi, \\ R_{21} &= \int C_I \cos 2\chi d\varphi, \\ R_{22} &= \int [C_+ \cos 2(\chi - \chi_1) + C_- \cos 2(\chi + \chi_1)] d\varphi, \end{aligned} \quad (\text{A5})$$

where  $C_{\pm} = (C_Q \pm C_U)/2$ , and the cosines are given by

$$\cos \chi = \frac{\mu_1 - \mu \cos \theta}{\sin \theta \sqrt{1 - \mu^2}}, \quad \cos \chi_1 = \frac{\mu - \mu_1 \cos \theta}{\sin \theta \sqrt{1 - \mu_1^2}}, \quad (\text{A6})$$

with  $\cos \theta = \mu\mu_1 + \sqrt{1-\mu^2}\sqrt{1-\mu_1^2} \cos \varphi$ . Finally, the functions  $C, C_I, C_Q$ , and  $C_U$  are four of the five functions forming the thermal Compton redistribution matrix,  $\hat{C}(x, x_1, \cos \theta)$ . This matrix is given by a single integral over the electron energy distribution  $f(\gamma)$  and the Compton redistribution matrix,  $\hat{C}^m(x, x_1, \cos \theta, \gamma)$ , for an isotropic *monoenergetic* electron gas with Lorentz factor  $\gamma$  (Nagirner & Poutanen 1993):

$$\begin{aligned} \hat{C}(x, x_1, \cos \theta) &= \begin{pmatrix} C & C_I & 0 & 0 \\ C_I & C_Q & 0 & 0 \\ 0 & 0 & C_U & 0 \\ 0 & 0 & 0 & C_V \end{pmatrix} \\ &= \frac{3}{8} \int_{\gamma_*}^{\infty} f(\gamma) \hat{C}^m(x, x_1, \cos \theta, \gamma) d\gamma = \frac{3}{8} \int_{\gamma_*}^{\infty} f(\gamma) d\gamma \begin{pmatrix} C^m & C_I^m & 0 & 0 \\ C_I^m & C_Q^m & 0 & 0 \\ 0 & 0 & C_U^m & 0 \\ 0 & 0 & 0 & C_V^m \end{pmatrix}, \end{aligned} \quad (\text{A7})$$

where

$$\gamma_* \equiv [x - x_1 + Q(1 + 2/q)^{1/2}]/2, \quad q \equiv xx_1(1 - \cos \theta), \quad Q^2 \equiv (x - x_1)^2 + 2q.$$

The function  $C^m$  is the scalar redistribution function derived by Jones (1968) (see also Coppi & Blandford 1990). We use the following expressions to calculate the five functions that enter  $\hat{C}^m(x, x_1, \cos \theta, \gamma)$  in equation (A7):

$$\begin{aligned} C^m &= C_a^m + C_b^m, \\ C_I^m &= C_a^m + C_c^m, \\ C_U^m &= \frac{2}{Q} + 2 \frac{u - Q}{rq} \left[ \frac{u - Q}{rq} (2Q + u) - 4 \right] + \frac{2u}{vq} + 2R_c^m, \\ C_Q^m &= C_U^m + C_a^m, \\ C_V^m &= C_b^m - qC_a^m, \end{aligned} \quad (\text{A8})$$

where

$$\begin{aligned} C_a^m &= u \frac{(u^2 - Q^2)(u^2 + 5v)}{2q^2v^3} + u \frac{Q^2}{q^2v^2}, \\ C_b^m &= \frac{2}{Q} + \frac{u}{v} \left( 1 - \frac{2}{q} \right), \\ C_c^m &= \frac{u}{vq} \left( \frac{u^2 - Q^2}{rq} - 2 \right), \end{aligned} \quad (\text{A9})$$

and

$$\begin{aligned} u &= a_1 - a = (x + x_1)(2\gamma + x_1 - x)/(a + a_1), & v &= aa_1, \\ a^2 &= (\gamma - x)^2 + r, & a_1^2 &= (\gamma + x_1)^2 + r, & r &= (1 + \cos \theta)/(1 - \cos \theta). \end{aligned} \quad (\text{A10})$$

The normalized relativistic Maxwellian distribution is given by

$$f(\gamma) = \frac{e^{-\gamma/\Theta}}{4\pi\Theta K_2(1/\Theta)}, \quad (\text{A11})$$

which gives the density of particles in the dimensionless momentum volume,  $4\pi z^2 dz$ , normalized to unity. Here,  $K_n$  is the modified Bessel function of second kind of order  $n$ , and  $z \equiv \sqrt{\gamma^2 - 1}$ . Methods for computing the integrals when averaging  $\hat{C}^m(x, x_1, \cos \theta, \gamma)$  over a relativistic Maxwellian electron distribution are given in Poutanen (1994). If the electron temperature is not very high ( $\Theta < 1$ ) we can use Gauss-Laguerre quadrature.

## A.2. The Compton Redistribution Function for Isotropic Scattering in the Electron Rest Frame

A very simple expression for the redistribution function,  $C^m$ , can be derived if we assume that the characteristic photon energy in the electron rest frame is small  $x_1\gamma \ll 1$ , i.e. the Thomson limit. The scattering in this limit can be assumed to be coherent in the electron rest frame. We also assume that the scattering is isotropic in the rest frame. Such simplifications give a correctly normalized redistribution function at energies  $x \ll \Theta$  (see eq. [A23]), whose shape slightly differs from the exact one. The function  $C^m$  in that approximation becomes (Arutyunyan & Nikogosyan 1980)

$$C^m = \frac{4}{3Q}, \quad (\text{A12})$$

being non-zero when

$$2q(\gamma^2 - 1) \geq (x_1 - x)^2. \quad (\text{A13})$$

Integration over  $\cos \theta$  between the limits defined by equation (A13) gives the angle-averaged redistribution function (Rybicki & Lightman 1979):

$$C^m(x, x_1, \gamma) = \int C^m \sin \theta d\theta = \frac{4}{3xx_1} \left[ x + x_1 - \frac{\gamma}{z} |x - x_1| \right], \quad (\text{A14})$$

where  $x/x_1 \in [(\gamma - z)^2, (\gamma + z)^2]$ . For Maxwellian electrons the redistribution function is given by

$$C(x, x_1, \cos \theta) = \frac{1}{8\pi Q} \frac{e^{-\gamma_*/\Theta}}{K_2(1/\Theta)}, \quad (\text{A15})$$

where  $\gamma_* = Q/\sqrt{2q}$ . Equation (A15) gives very good approximation to the exact redistribution function for mildly relativistic temperatures and  $x \ll \Theta$ . Notice also that  $xC(x, x_1, \cos \theta)$  is a function of the ratio  $x/x_1$ . In Table 1 this approximation is called ISOSCAT1. Even better agreement with the exact redistribution function is obtained if  $\gamma_*$  from equation (A8) is used in equation (A14). We call this approximation ISOSCAT2 in Table 1. The accuracy of these approximations is discussed in § 5.2.

### A.3. The Thermally Averaged Compton Scattering Cross Section

The Compton scattering cross section averaged over a relativistic Maxwellian electron distribution can be written as an integral over the electron energy:

$$\begin{aligned}\sigma_{\text{cs}}(x) &= \frac{3\sigma_T}{16x^2\Theta K_2(1/\Theta)} \int_1^\infty e^{-\gamma/\Theta} \left[ \left( x\gamma + \frac{9}{2} + \frac{2}{x}\gamma \right) \ln \frac{1+2x(\gamma+z)}{1+2x(\gamma-z)} - 2xz \right. \\ &+ \left. z \left( x - \frac{2}{x} \right) \ln(1+4x\gamma+4x^2) + \frac{4x^2z(\gamma+x)}{1+4x\gamma+4x^2} - 2 \int_{x(\gamma-z)}^{x(\gamma+z)} \ln(1+2\xi) \frac{d\xi}{\xi} \right] d\gamma \quad (A16)\end{aligned}$$

Making the substitutions  $\gamma = 1 + \Theta \exp(-2t)$  on the interval  $[1, 1 + \Theta]$ , and  $\gamma = 1 + \Theta(1 + t)$  on the interval  $[1 + \Theta, \infty)$ , and applying 10-points Gauss-Laguerre quadrature formula we achieve an accuracy better than 0.02 per cent.

In limiting cases, the thermal cross section can be computed using simple expressions (Gould 1982; Svensson 1982; Nagirner & Poutanen 1994):

$$\sigma_{\text{cs}}(x) = \frac{3\sigma_T}{8x^2} \left[ 4 + \left( x - 2 - \frac{2}{x} \right) \ln(1+2x) + \frac{2x^2(1+x)}{(1+2x)^2} \right], \quad \Theta \ll 1, \quad (A17)$$

$$\sigma_{\text{cs}}(x) = \frac{3\sigma_T}{16x\Theta} \left( \frac{1}{2} - \gamma_E + \ln 4x\Theta \right), \quad \Theta \gg 1, x\Theta \gg 1, \quad (A18)$$

$$\sigma_{\text{cs}}(x) = \frac{\sigma_T}{K_2(1/\Theta)} \sum_{n=0}^{\infty} (-2x)^n a_n K_{n+2}(1/\Theta), \quad x\Theta \ll 1, \quad (A19)$$

where

$$a_n = \frac{3}{8} \left[ n+2 + \frac{2}{n+1} + \frac{8}{n+2} - \frac{16}{n+3} \right]. \quad (A20)$$

These simple approximations can be used to check the correctness of the thermal cross section routine and to estimate the numerical accuracy.

### A.4. Symmetry Properties and a Normalization Condition

The azimuth and thermally averaged functions  $R_{ij}$  have symmetry properties which can be exploited to simplify the radiative transfer equation, to reduce the time needed to calculate all elements of the redistribution matrix, and to check the accuracy of the calculations:

#### 1. Frequency symmetry

$$R_{ij}(x, \mu; x_1, \mu_1) e^{-x_1/\Theta} = R_{ij}(x_1, \mu; x, \mu_1) e^{-x/\Theta}, \quad i, j = 1, 2, \quad (A21)$$

which follows from microscopic detailed balance between states  $x$  and  $x_1$  when the photons and the electrons have a Wien and a Maxwellian distribution, respectively (Pomraning 1973; Mészáros & Bussard 1986). The exponential factors represent the Wien distribution, while the photon phase space factors have been absorbed in the definition of  $R_{ij}$ .

## 2. Angular symmetry

$$\begin{aligned} R_{ij}(x, \mu; x_1, \mu_1) &= R_{ji}(x, \mu_1; x_1, \mu), \\ R_{ij}(x, \mu; x_1, \mu_1) &= R_{ij}(x, -\mu; x_1, -\mu_1), \quad i, j = 1, 2. \end{aligned} \quad (\text{A22})$$

These angular symmetries follow directly from the fact that the scattering process depends on the scattering angle between the in and outgoing photons, and not on their angle cosines,  $\mu$  and  $\mu_1$ , separately.

The thermal Compton scattering cross section,  $\sigma_{\text{cs}}(x)$ , and the scalar redistribution function,  $R_{11}(x_1, \mu_1; x, \mu)$ , i.e. element 11 of the thermal redistribution matrix, are related through a normalization condition (see e.g. Pomraning 1973; Nagirner & Poutanen 1994):

$$\frac{\sigma_{\text{cs}}(x)}{\sigma_T} = \frac{1}{x} \int_0^\infty x_1 dx_1 \int_0^1 d\mu \int_0^1 d\mu_1 [R_{11}(x_1, \mu_1; x, \mu) + R_{11}(x_1, \mu_1; x, -\mu)]. \quad (\text{A23})$$

Analogous integrations of  $R_{12}$  and  $R_{21}$  gives zero on the left hand side due to the requirement that the polarization is zero ( $Q = 0$ ) for an isotropic radiation field. These relations can be used to check the accuracy of the calculation of the redistribution matrix, and to estimate the quality of the frequency and the angular discretization.

## A.5. The Photon-Photon Pair Production Rate

For azimuth-independent (i.e. axisymmetric) photon distributions, the rate of photon-photon pair production,  $\dot{n}_{\gamma\gamma}$  cm $^{-3}$  s $^{-1}$ , neglecting polarization is given by integrals over dimensionless photon energy,  $dx$ , and solid angle,  $2\pi d\mu$ , as follows:

$$\dot{n}_{\gamma\gamma}(\tau) = \frac{1}{2} \frac{2\pi}{m_e c^2} \int_0^\infty \frac{dx}{x} \int_{-1}^1 I(\tau, x, \mu) \alpha_{\gamma\gamma}(\tau, x, \mu) d\mu. \quad (\text{A24})$$

Here,  $I(\tau, x, \mu)dx/(cm_e c^2 x)$  is the number density of photons of energy  $x$  in the interval  $dx$  per steradian traveling in the direction  $\mu$ , and  $\alpha_{\gamma\gamma}$  cm $^{-1}$  is the absorption coefficient due to photon-photon pair production. The factor 1/2 is due to both interacting species being photons. The absorption coefficient is given by another integral over the target photon energy,  $dx_1$ , and solid angle,  $d\varphi d\mu_1$ ,

$$\alpha_{\gamma\gamma}(\tau, x, \mu) = \frac{r_e^2}{m_e c^3} \int_0^\infty \frac{dx_1}{x_1} \int_{-1}^1 R_{\gamma\gamma}(x, \mu; x_1, \mu_1) I(\tau, x_1, \mu_1) d\mu_1, \quad (\text{A25})$$

where  $r_e$  is the classical electron radius,  $R_{\gamma\gamma}(x, \mu; x_1, \mu_1)$  is the dimensionless, azimuth-integrated pair production cross section,

$$R_{\gamma\gamma}(x, \mu; x_1, \mu_1) = 2 \int_{\varphi_{\min}}^{\pi} s_{\gamma\gamma}(\omega) (1 - \cos \theta) d\varphi, \quad (\text{A26})$$

the  $(1 - \cos \theta)$  factor is discussed in, e.g., Weaver (1976), and  $s_{\gamma\gamma}(\omega)$  is the dimensionless photon-photon pair production cross section (Jauch & Rohrlich 1976)

$$s_{\gamma\gamma}(\omega) \equiv \frac{\sigma_{\gamma\gamma}(\omega)}{r_e^2} = \frac{\pi}{\omega} \left[ \left( 2 + \frac{2}{\omega} - \frac{1}{\omega^2} \right) \cosh^{-1} \sqrt{\omega} - \left( 1 + \frac{1}{\omega} \right) \sqrt{1 - \frac{1}{\omega}} \right]. \quad (\text{A27})$$

Here,  $\omega \equiv x_{cm}^2 = xx_1(1 - \cos \theta)/2$ , where  $x_{cm}$  is the photon energy in the center-of-momentum frame, and  $\theta$  is the interaction angle related to other cosines as  $\cos \theta = \mu\mu_1 + \sqrt{1 - \mu^2}\sqrt{1 - \mu_1^2} \cos \varphi$ . Using these relations, the threshold condition for pair production,  $x_{cm} > 1$ , can be written as a constraint on  $\cos \theta$  or on  $\cos \varphi$  giving a minimum allowed value for  $\varphi$ :  $\cos \varphi_{\min} = (1 - \mu\mu_1 - 2/xx_1)/(\sqrt{1 - \mu^2}\sqrt{1 - \mu_1^2})$ . The factor 2 in equation (A26) comes from the integration range originally being  $\varphi_{\min}$  to  $2\pi - \varphi_{\min}$ , and the integrand being an even function of  $\varphi$  around  $\varphi = \pi$ . The axisymmetric pair production rate was previously considered by Stepney & Guilbert (1983) who chose  $x_{cm}$  as integration variable instead of  $\varphi$ . Their rate is a factor 2 too large as pointed out by Kusunose (1987).

### A.6. The Thermal Pair Annihilation Rate

For a relativistic Maxwellian electron (and positron) distribution, the pair annihilation reaction rate,  $\dot{n}_{\text{ann}} \text{ cm}^{-3} \text{ s}^{-1}$ , can be written as a one-parameter ( $\Theta$ ) single integral (Weaver 1976). Svensson (1982) made a simple fit to that integral accurate to within 2 per cent:

$$\dot{n}_{\text{ann}} = n_- n_+ c r_e^2 \frac{\pi}{1 + 2\Theta^2 / \ln(1.3 + 2\eta_E \Theta)}, \quad (\text{A28})$$

where  $\eta_E \approx 0.5615$ .

### A.7. Pair Annihilation Emissivity

The emissivity due to thermal pair annihilation,  $\epsilon_{\text{ann}}(x, \Theta) dx \text{ erg cm}^{-3} \text{ s}^{-1} \text{ sr}^{-1}$ , in an energy interval  $dx$  can be written using detailed balance arguments in terms of the pair production cross section in the following form (Svensson 1983):

$$\epsilon_{\text{ann}}(x, \Theta) = n_- n_+ r_e^2 m_e c^3 \frac{x e^{-x/\Theta}}{2\pi\Theta K_2^2(1/\Theta)} \int_1^\infty \omega s_{\gamma\gamma}(\omega) e^{-\omega/x\Theta} d\omega, \quad (\text{A29})$$

where  $s_{\gamma\gamma}(\omega)$  is given by equation (A27). Simple analytical fits for the one-parameter ( $x\Theta$ ) integral in equation (A29) accurate to within 0.04 per cent are given by Svensson, Larsson, & Poutanen (1996).

### A.8. Symmetry Properties of the Azimuth-integrated Pair Production Cross Section

The azimuth-integrated cross section,  $R_{\gamma\gamma}$ , obey energy and angular symmetry relations, which are useful in reducing the computing time:

$$\begin{aligned} R_{\gamma\gamma}(x, \mu; x_1, \mu_1) &= R_{\gamma\gamma}(xx_1, \mu, \mu_1), \\ R_{\gamma\gamma}(x, \mu; x_1, \mu_1) &= R_{\gamma\gamma}(x, \mu_1; x_1, \mu), \\ R_{\gamma\gamma}(x, \mu; x_1, \mu_1) &= R_{\gamma\gamma}(x, -\mu; x_1, -\mu_1). \end{aligned} \quad (\text{A30})$$

These symmetry relations follow directly from equation (A26), the definition of  $\omega$ , and the relations for  $\cos\theta$  and  $\cos\varphi_{\min}$ . To check the accuracy of our calculations we integrate the azimuth-integrated cross section over one cosine angle and average over the second in order to obtain the fully solid angle-integrated cross section for the isotropic case (which is a well known function first computed by Gould and Schréder 1967):

$$R_{\gamma\gamma}^{\text{iso}}(xx_1) = \frac{1}{2} \int_{-1}^1 d\mu \int_{-1}^1 d\mu_1 R_{\gamma\gamma}(x, \mu; x_1, \mu_1) = \int_0^1 d\mu \int_0^1 d\mu_1 [R_{\gamma\gamma}(x, \mu; x_1, \mu_1) + R_{\gamma\gamma}(x, \mu; x_1, -\mu_1)]. \quad (\text{A31})$$

Here we have used the third symmetry property above. The angle-averaged function,  $\bar{\phi}(xx_1)$  in Gould & Schréder (1967) is related to our  $R_{\gamma\gamma}^{\text{iso}}(xx_1)$  through  $\bar{\phi}(xx_1) = (xx_1)^2 R_{\gamma\gamma}^{\text{iso}}(xx_1)/8\pi^2$ . The angle-averaged cross section,  $R(xx_1)$  in Coppi & Blandford (1990), is related to our  $R_{\gamma\gamma}^{\text{iso}}(xx_1)$  through  $R(xx_1) = cr_e^2 R_{\gamma\gamma}^{\text{iso}}(xx_1)/(4\pi)$ . Coppi & Blandford (1990) give a useful fit for  $R(xx_1)$  accurate to within 7 per cent for all  $xx_1$ . We find our  $R_{\gamma\gamma}^{\text{iso}}(xx_1)$  computed using equation (A31) to typically be accurate to within 2 per cent.

One can show that the annihilation emissivity can be written as an integral, not over the pair production cross section, but over the angle-integrated pair production cross section:

$$\epsilon_{\text{ann}}(x, \Theta) = n_- n_+ r_e^2 m_e c^3 \frac{x^3 e^{-x/\Theta}}{16\pi^2 \Theta^2 K_2^2(1/\Theta)} \int_0^\infty x_1^2 R_{\gamma\gamma}^{\text{iso}}(xx_1) e^{-x_1/\Theta} dx_1. \quad (\text{A32})$$

By numerically computing this integral using our computed  $R_{\gamma\gamma}^{\text{iso}}(xx_1)$  and comparing with equation (A29) we obtain an extra check of the consistency of our pair production and annihilation routines.

### A.9. Double Compton emissivity

The angle-averaged double Compton spectral emissivity,  $\epsilon_{\text{DC}}(x, \Theta) dx$  erg cm<sup>-3</sup> s<sup>-1</sup> sr<sup>-1</sup>, in an energy interval  $dx$  is given by the expression (see, e.g., Svensson 1984):

$$\epsilon_{\text{DC}}(x, \Theta) = (n_+ + n_-) x \frac{e^{-x/\Theta}}{2K_2(1/\Theta)} \int_0^\infty x_1^{-3} J(x_1) dx_1 \int_0^\infty \omega \frac{d\sigma_{\text{DC}}}{dx}(x, \omega) \exp\left(-\frac{\omega/x_1 + x_1/\omega}{2\Theta}\right) d\omega. \quad (\text{A33})$$

Here  $J(x_1)$  is the mean intensity of the interacting photons. The differential cross section for the double Compton process is given in Svensson (1984, eqs. [A5], [A6]). In order to account for the high energy cutoff at  $x > \Theta$  we introduced an *ad hoc* exponential factor,  $e^{-x/\Theta}$ .

### A.10. Bremsstrahlung emissivity

The emissivities due to relativistic electron-electron and positron-positron thermal bremsstrahlung,  $\epsilon_{\pm\pm}(x, \Theta)dx$  erg cm<sup>-3</sup> s<sup>-1</sup> sr<sup>-1</sup>, in an energy interval  $dx$  are given by the expression:

$$\epsilon_{\pm\pm}(x, \Theta) = n_{\pm} n_{\pm} \sigma_T \alpha_f m_e c^3 e^{-x/\Theta} \Theta^{-1/2} \frac{2^{3/2}}{3\pi} g_{\pm\pm}(x, \Theta). \quad (\text{A34})$$

A similar expression holds for the electron-positron emissivity  $\epsilon_{+-}(x, \Theta)$ . We used the approximations by Skibo et al. (1995) for the Gaunt factors  $g_{\pm\pm}(x, \Theta)$  and  $g_{+-}(x, \Theta)$ . Note that the term of unity in equations (A7), (A9), and (A13) in Skibo et al. (1995) should be deleted.

### A.11. Numerical Integration

All azimuthal integrations are made using an 11-point Simpson quadrature. Furthermore, we apply 3-point Gaussian quadrature to calculate integrals over zenith angles for each hemisphere. The integration over frequencies is performed using rectangular quadrature on a logarithmic frequency scale,  $dx/x = d \ln x$ , with bin width  $\sim 0.1$ . The integrals over optical depth are calculated using rectangular quadrature. The number of points,  $N_\tau$ , is dependent on the geometry and the optical depth. We typically used  $N_\tau = 6$  for slabs, and  $N_\tau = 11 - 21$  for active regions.

Table 1. Comparison of results obtained using the ISM and NLNC codes.

Method	SLAB			HEMISPHERE		
	$\Theta$	$\tau_T$	$l_{\text{diss}}$	$\Theta$	$\tau_T$	$l_{\text{diss}}$
ISM	0.19	0.29	260	0.24	0.70	560
NLNC	0.19	0.29	300	0.24	0.70	700
ISOSCAT1	0.19	0.29	1830	0.24	0.70	2730
ISOSCAT2	0.19	0.29	390	0.24	0.70	740
ISORAD	0.19	0.29	250	0.24	0.70	470
ISOSF	0.19	0.30	340	0.24	0.76	640
ISM	0.29	0.17	19	0.49	0.29	27
NLNC	0.29	0.16	20	0.49	0.28	40
ISOSCAT1	0.29	0.17	86	0.49	0.29	70
ISOSCAT2	0.29	0.17	25	0.49	0.29	32
ISORAD	0.29	0.17	17	0.49	0.29	20
ISOSF	0.29	0.17	23	0.49	0.30	31
ISM	0.82	0.036	0.24	1.20	0.073	1.5
NLNC	0.82	0.033	0.20	1.20	0.070	3.0
ISOSCAT1	0.82	0.037	0.47	1.20	0.076	2.4
ISOSCAT2	0.82	0.036	0.27	1.20	0.073	1.6
ISORAD	0.82	0.036	0.16	1.20	0.073	0.8
ISOSF	0.82	0.036	0.27	1.20	0.075	1.6

Input parameter:  $\Theta \equiv kT_e/m_e c^2$ , the dimensionless pair temperature of the corona (volume averaged in the NLNC case); Output parameters:  $\tau_T$ , the (averaged) Thomson optical depth;  $l_{\text{diss}} \equiv (L_{\text{diss}}/H)(\sigma_T/m_e c^3)$ , the local dissipation compactness of the coronal slab or hemisphere. In all cases,  $d = 0$  and  $T_{\text{bb}} = 5$  eV. ISM and NLNC represent results using the ISM and NLNC codes, respectively. ISOSCAT1 and ISOSCAT2 represent ISM results using isotropic scattering in the electron rest frame (Appendix A2). ISORAD represent ISM results when the radiation field is made isotropic before solving the pair balance. ISOSF represent ISM results when the source functions,  $S_{k \geq 2}$ , are assumed to be isotropic and homogeneous (see § 3.4).

Code	$\Theta$	$\tau_T$	$l_{\text{diss}}$	$\alpha_{2-18}$		
ISM				$\mu = 0.113$	$\mu = 0.5$	$\mu = 0.887$
HM93				$\mu = 0.15$	$\mu = 0.55$	$\mu = 0.95$
ISM	0.26	0.19	34	1.15	1.11	1.08
HM93	0.26	0.20	22	1.23	1.14	1.10
ISM	0.67	0.05	0.49	0.89	0.77	0.69
HM93	0.67	0.05	2	0.87	0.73	0.65
ISM	1.75	0.01	0.02	1.37	1.16	0.85
HM93	1.75	0.01	0.1	1.23	0.95	0.53

Table 2: Comparison of ISM results for coronal slabs with those of HM93

---

Note. — Input parameter:  $\Theta \equiv kT_e/m_e c^2$ , the dimensionless pair temperature of the coronal slab; Output parameters:  $\tau_T$ , the vertical Thomson optical depth of the coronal slab;  $l_{\text{diss}} \equiv (L_{\text{diss}}/H)(\sigma_T/m_e c^3)$ , the dissipation compactness of the coronal slab;  $\alpha_{2-18}$ , the least square fitted 2-18 keV intensity slope for three specified cosine angles. In all cases,  $d = 0$  and  $T_{\text{bb}} = 5$  eV. See text for determination of  $l_{\text{diss}}$  from HM93.

## REFERENCES

Antonucci, R. 1993, *ARA&A*, 31, 473

Arutyunyan, G. A., & Nikogosyan, A. G. 1980, *Sov. Phys. Doklady*, 25, 918

Chandrasekhar, S. 1960, *Radiative Transfer* (New York: Dover)

Coppi, P. S., & Blandford, R. D. 1990, *MNRAS*, 245, 453

Done, C., Mulchaey, J. S., Mushotzky, R. F., & Arnaud, K. A. 1992, *ApJ*, 395, 275

Gilfanov, M., et al. 1994, *ApJS*, 92, 411

Gould, R. J. 1982, *ApJ*, 254, 755

Gould, R. J., & Schréder, G.P. 1967, *Phys. Rev.*, 155, 1404

Haardt, F. 1993, *ApJ*, 413, 680

Haardt, F. 1994, Ph.D. thesis, SISSA, Trieste

Haardt, F., & Maraschi, L. 1991, *ApJ*, 380, L51

Haardt, F., & Maraschi, L. 1993, *ApJ*, 413, 507 (HM93)

Haardt, F., & Matt, G. 1993, *MNRAS*, 261, 346

Haardt, F., Maraschi, L., & Ghisellini, G. 1994, *ApJ*, 432, L95

Hua, X.-M., & Titarchuk, L. 1995, *ApJ*, 449, 188

Jauch, J. M. & Rohrlich, F. 1976, *The Theory of Photons and Electrons*, 2d ed. (New York: Springer-Verlag)

Jones, F. C. 1968, *Phys. Rev.*, 167, 1159

Kaaret, P., et al. 1992, *Columbia Astrophysics Laboratory Contribution No.* 469

Kusunose, M. 1987, *ApJ*, 321, 186

Madejski, G. M. et al. 1995, *ApJ*, 438, 672

Magdziarz, P., & Zdziarski, A. A. 1995, *MNRAS*, 273, 837

Matt, G. 1993, *MNRAS*, 260, 663

Mészáros, P., & Bussard, R. W. 1986, *ApJ*, 306, 238

Mushotzky, R. F., Done, C., & Pounds, K. A. 1993, *ARA&A*, 31, 717

Nagirner, D. I., & Poutanen, J. 1993, *A&A*, 275, 325

Nagirner, D. I., & Poutanen, J. 1994, in *Astrophys. & Space Phys. Reviews*, Vol. 9, ed. R. A. Sunyaev (New York: Harwood), 1

Nandra, K., & Pounds, K. A. 1994, *MNRAS*, 268, 405

Phillips, K. C., & Mészáros, P. 1986, *ApJ*, 310, 284

Pietrini, P., & Krolik, J. H. 1995, *ApJ*, 447, 526

Pomraning, G. S. 1973, The Equation of Radiation Hydrodynamics (Oxford: Pergamon Press)

Poutanen, J. 1994, *JQSRT*, 51, 813

Poutanen, J., & Vilhu, O. 1993, *A&A*, 275, 337

Poutanen, J., Nagendra, K. N., & Svensson, R. 1996, *MNRAS*, submitted

Rybicki, G.B., & Lightman, A.P. 1979, Radiative Processes in Astrophysics (New York: Wiley)

Skibo, J. G., Dermer, C. D., Ramaty, R., & McKinley, J. M. 1995, *ApJ*, 446, 86

Stepney, S., & Guilbert, P. W. 1983, *MNRAS*, 204, 1269

Stern, B. E., Begelman, M. C., Sikora, M., & Svensson, R. 1995a, *MNRAS*, 272, 291

Stern, B. E., Poutanen, J., Svensson, R., Sikora, M., & Begelman, M. C. 1995b, *ApJ*, 449, L13

Sunyaev, R. A. & Titarchuk, L. G. 1980, *A&A*, 86, 121

Sunyaev, R. A. & Titarchuk, L. G. 1985, *A&A*, 143, 374

Svensson, R. 1982, *ApJ*, 258, 321

Svensson, R. 1983, *ApJ*, 270, 300

Svensson, R. 1984, *MNRAS*, 209, 175

Svensson, R., Larsson, S., & Poutanen, J. 1996, *A&AS*, submitted

Tanaka, Y., & Levin, W. H. G. 1995, in Cambridge Astrophysics Series, Vol. 26, X-ray Binaries, eds. W. H. G. Levin, J. van Paradijs, & E. P. J. van den Heuvel (Cambridge: Cambridge University Press), 126

Titarchuk, L. 1994, *ApJ*, 434, 570

Weaver, T. A. 1976, *Phys. Rev.*, A13, 1563

White, T. R., Lightman, A. P., & Zdziarski, A. A. 1988, *ApJ*, 331, 939

Zdziarski, A. A. 1985, *ApJ*, 289, 514

Zdziarski, A. A. et al. 1994, *MNRAS*, 269, L55

Zdziarski, A. A., Johnson, W. N., Done, C., Smith, D., & McNaron-Brown, K., 1995, *ApJ*, 438, L63

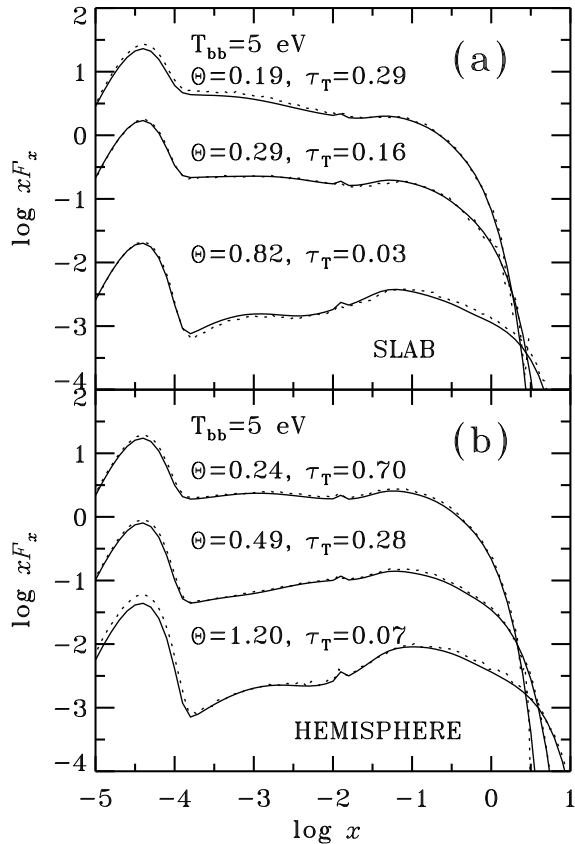


Fig. 1.— (a) Emergent flux,  $xF_x$  (arbitrary units), from slab pair coronae as function of dimensionless photon energy,  $x \equiv h\nu/m_ec^2$ , for the parameters in Table 1. The spectra are averaged over viewing angles  $0.6 < \mu < 0.9$ . *Solid and dotted curves*: results using the ISM code and NLMC code, respectively. (b) Same as (a), but for hemisphere coronae.

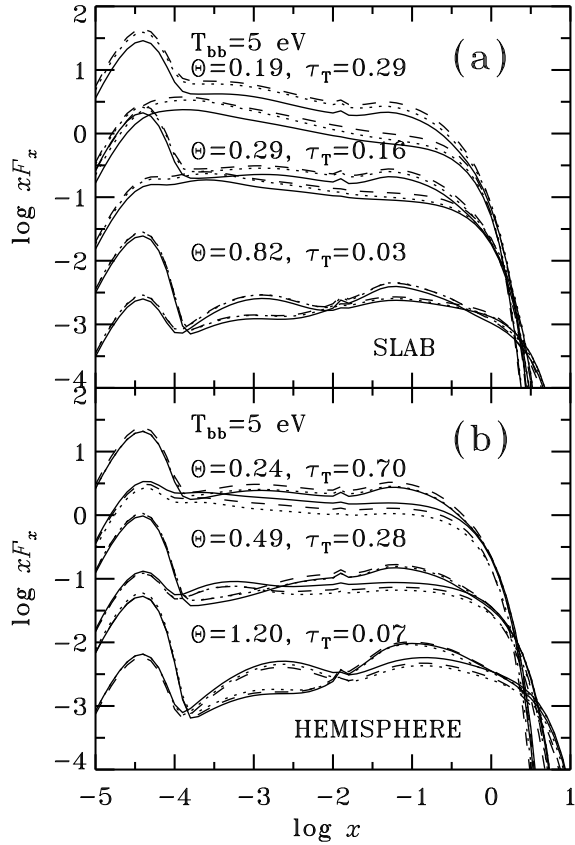


Fig. 2.— Same as Figure 1 but for two viewing angles,  $\mu = 0.11$  and  $\mu = 0.89$ . The face-on spectra ( $\mu = 0.89$ ) can be identified by their more prominent black body component. All curves represent results from the ISM code. Results using the exact scattering kernel are shown by *solid curves*. *Dashed curves* represent results assuming isotropic scattering in the electron rest frame (ISOSCAT2, see Appendix A2). *Dotted curves* correspond to the isotropic source function approximation (ISOSF). Notice that the emergent spectra for the different approximations are normalized to the corresponding value of  $l_{\text{diss}}$  in Table 1. The spectral fluxes in a given direction differ slightly, but the spectral shapes are almost identical.

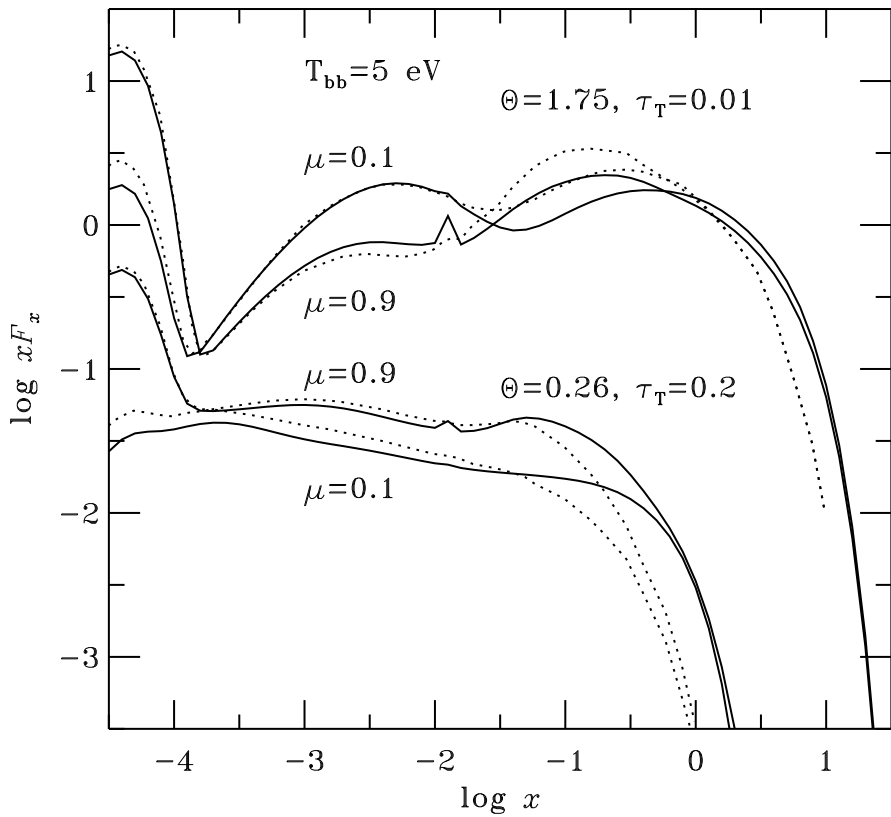


Fig. 3.— Emergent flux,  $xF_x$  (arbitrary units), from slab pair coronae as function of dimensionless photon energy,  $x \equiv h\nu/m_ec^2$ . *Solid curves*: results using the ISM code for  $\mu = 0.11$  and  $\mu = 0.89$ . *Dotted curves*: results from Figures 4a,c in HM93 for  $\mu = 0.15$  and  $\mu = 0.95$ .

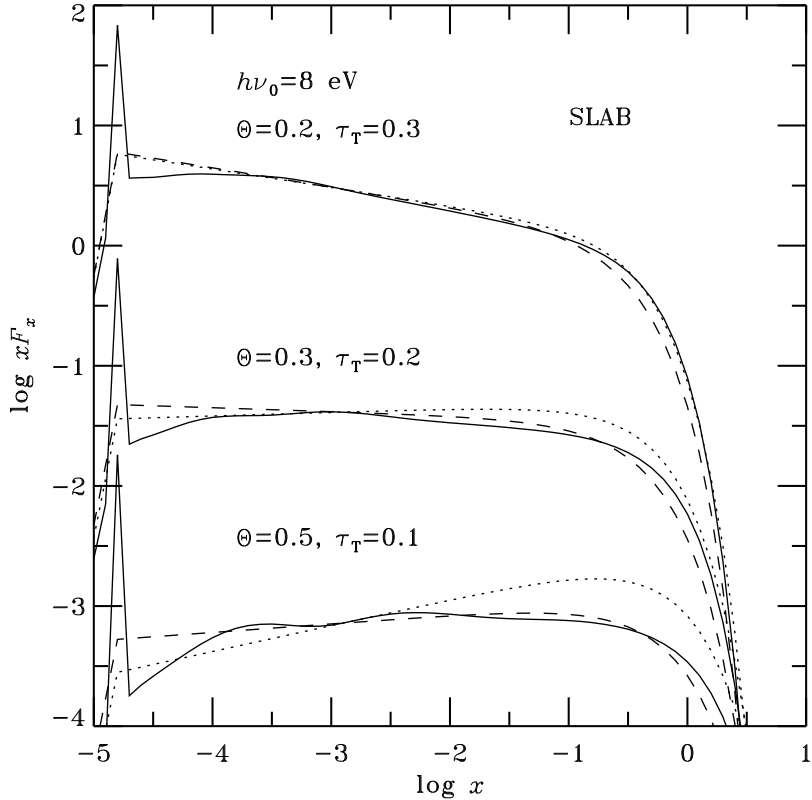


Fig. 4.— Angle averaged Comptonized spectra,  $x F_x$  (arbitrary units), from slab coronae as function of dimensionless photon energy,  $x \equiv h\nu/m_e c^2$ . Soft monochromatic photons with  $h\nu_0 = 8 \text{ eV}$  are assumed to be incident on the lower boundary of the slab. *Solid curves*: results using the ISM code; *dotted curves*: spectra using the analytical formulae (35) and (44) from Titarchuk (1994); *dashed curves*: spectra using the analytical formulae (9) and (10) from Hua & Titarchuk (1995). No pair or energy balance is imposed.

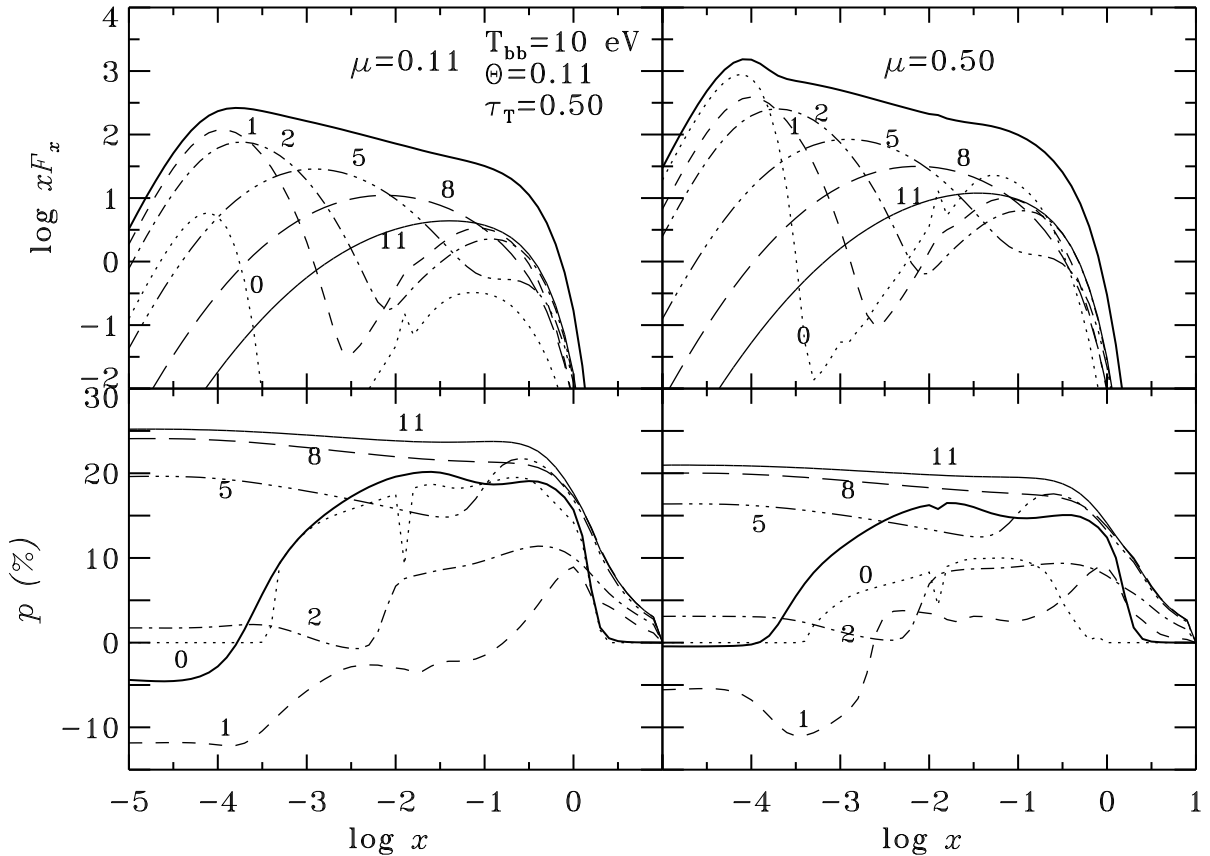


Fig. 5.— Emergent flux,  $xF_x$ , from slab coronae (upper panels) and the degree of polarization,  $p$  (lower panels) as function of dimensionless photon energy,  $x \equiv h\nu/m_ec^2$ , for  $\Theta = 0.11$ ,  $\tau_T = 0.50$ ,  $T_{bb} = 10$  eV for two viewing angles  $\mu = 0.11$  and  $\mu = 0.50$ . No pair or energy balance is imposed. *Thick solid curves*: the overall spectra and polarization. The contribution from some of the scattering orders is also shown. The labels show the order of scattering. The zeroth (*dotted*) component consists of the unpolarized blackbody disk radiation as well as the radiation reflected from the cold disk. The scattered components consist of multiple scattered blackbody radiation and multiple scattered reflected radiation with the latter being centered around  $x \sim 0.1$ .

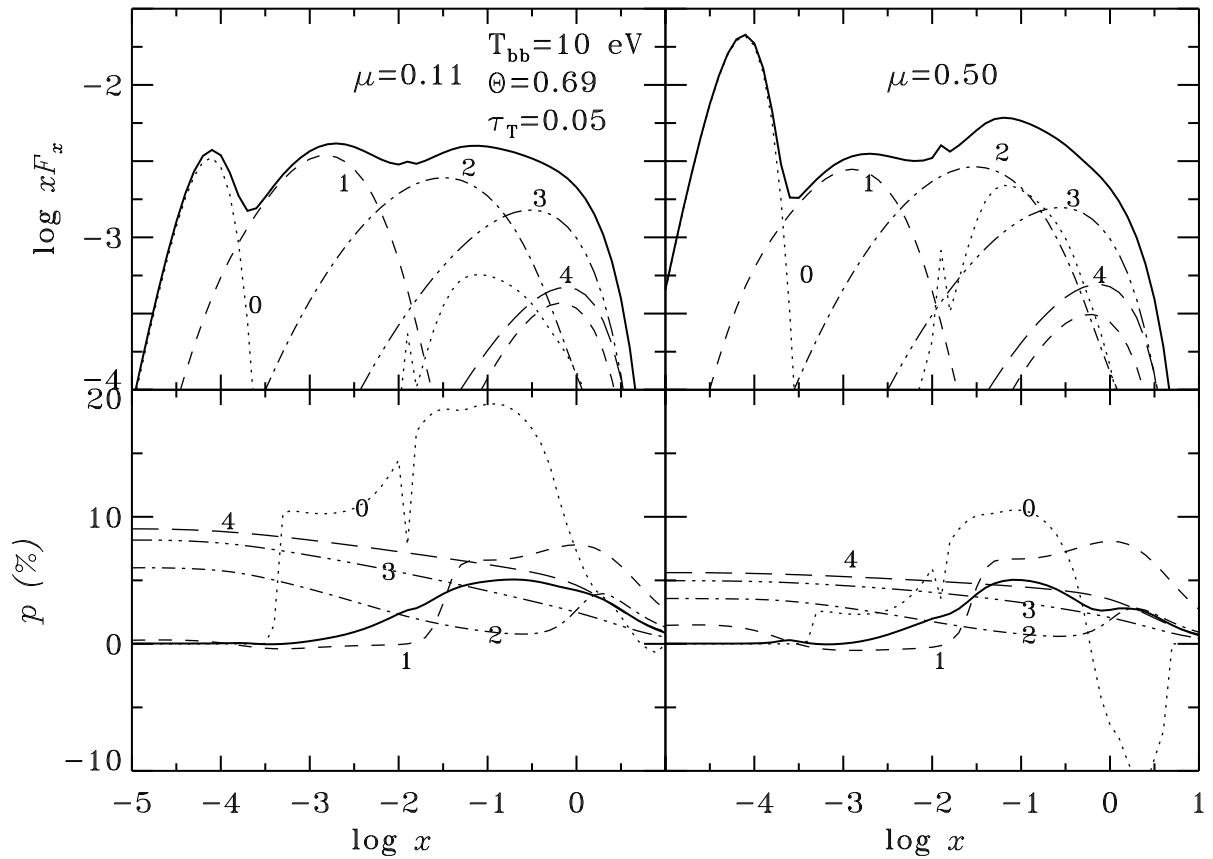


Fig. 6.— Same as Figure 5 but for  $\tau_T = 0.05$  and  $\Theta = 0.69$ .